N84-20970

The upper mantle beneath the Cascade Range: a comparison with the Gulf of California

Marianne C. Walck

Seismological Laboratory, California Institute of Technology,
Pasadena, CA 91125

March 16, 1984

Abstract

Seismograms from 22 earthquakes along the northeast Pacific rim recorded in southern California form the data set for investigation of the upper mantle beneath the Cascade Range-Juan de Fuca region, a transitional area encompassing both very young ocean floor and a continental margin. These data consist of 853 seismograms ($6^\circ < \Delta < 42^\circ$) which produce 1068 travel times and 40 ray parameter estimates. We compare these data directly to another large suite of records representative of structure beneath the Gulf of California, an active spreading center (Walck, 1984). We use the spreading center model, GCA, as a starting point in WKBJ synthetic seismogram modeling and perturb GCA until the northeast Pacific data are matched. Application of wave field continuation (Clayton & McMechan, 1981; Walck & Clayton, 1984) to these two groups of data provides checks on model's consistency with the data as well as an estimate of the resolvability of differences between the two areas. Differences between the models derived from these two data sets are interpretable in terms of lateral structural variation beneath the two regimes. Significant disparities in travel times and waveforms from 16° to 22° imply corresponding velocity variations between the two regions from 200-410 km depth. The ocean-continent transition model, CJF, features velocities from 200 and 350 km that are intermediate

between the very low values of GCA and the more moderate values of T7 (Burdick & Helmberger, 1978), a model for the inland western United States. Models of continental shield regions (e.g., King & Calcagnile, 1976) have even higher velocities in this depth range, but all four model types are similar below 450 km. This regular pattern observed in the rate of velocity increase with tectonic regime suggests an inverse relationship between velocity gradient and lithospheric age above 400 km depth.

Introduction

An accurate global assessment of the upper mantle velocity distribution is important in solving many key geophysical problems. Assembling such a world-wide map is not straightforward because the widely varying methods and types of data used in regional studies are difficult to compare directly. The ideal upper mantle experiment might involve multiple identical three-component, broad-band seismic arrays cleverly situated within 30° distance of every major seismic zone. The lack of such instrumentation forces us to consider an alternate method: identical analysis of multiple data sets, facilitating structural comparison between regions. Burdick (1981) and Grand & Helmberger (1984) model long-period P and SS waves, respectively, with synthetic seismograms and establish gross structural differences between continental shields and tectonically active continental areas. Burdick (1981) presents two models which separate only in the uppermost 250 km. The shear wave models of Grand & Helmberger (1984), however, are disparate to 400 km depth. Their tectonic model, TNA, is in excellent agreement with the P-wave spreading center model, GCA, developed in Walck (1984), hereafter referred to as Paper I.

Wiggins & Helmberger (1973) and Dey-Sarkar & Wiggins (1976) compare smaller regions within midwestern and western North America using synthetic seismogram modeling of short-period P waves recorded from several source regions at widely separated receivers. The two models for the United States, HWA and HWB (Wiggins & Helmberger, 1973) disagree to depths of over 400 km. Dey-Sarkar & Wiggins (1976) propose three varying models for areas of northwest Canada; their model discrepancies are mostly in lithospheric thickness and in the shapes of low-velocity zones. Because the data types and

analysis are identical, these models are directly comparable and document lateral variations within the North American continent.

For a conveniently located seismic array, comparative studies of the upper mantle are straightforward. We can record events in the proper distance ranges from several azimuths and process the data uniformly to obtain good estimates of the model changes required by the data. Niazi & Anderson (1965) utilize earthquakes from two azimuths in their data collected at the Tonto Forest Seismological Observatory (TFSO) in Arizona. While they have insufficient data to conduct separate analyses, the $dT/d\Delta$ measurements from both source areas are consistent. Johnson (1967), also using TFSO, similarly combines multi-azimuth data sets into one upper mantle model.

Several investigators have directly compared data collected from similar distances but differing azimuths at a single array. England et al. (1978) contrast P waves traveling beneath the North Atlantic and Arctic oceans to those bottoming under Russia and central Europe. Ram & Mereu (1977) probe the upper mantle in four different regions using the Gauribidanur array in southern India. While neither study employs waveform modeling, the travel time and p-Δ data from the different areas are dissimilar enough to document significant structural variations between the oceanic and continental source regions. At YKA, Ram et al. (1978) study the lateral variations in the upper mantle to the west and south of that northern Canadian array. Their extreme data scatter precludes strong statements about absolute velocities, yet once again the two data groups are quantitatively different, indicating lateral velocity gradients within the mantle.

The addition of waveform modeling techniques to the dense array data should aid in identification and documentation of even subtle structural variations between regions. SCARLET, the Caltech-U.S. Geological Survey southern California seismic network, is conveniently located between two seismically active zones on the Pacific Ocean rim. Paper I reports on the results of modeling upper mantle velocities beneath the Gulf of California spreading center, derived from data recorded from Mexican events. Velocities under the ridge are low compared with other models to depths of 350 km. Significant seismic activity also occurs to the northwest of southern California at appropriate distances for upper mantle study, from northern California to Alaska. Energy from these events arriving at SCARLET is especially sensitive to velocities under the Cascade Range of Oregon and Washington and the Juan de Fuca plate (Figure 1a). The Cascade Range represents Quaternary volcanism related to subduction, and the Juan de Fuca plate is very young oceanic crust. The disparities between this tectonically active region and the Gulf of California, therefore, may not be as dramatic as those between continental shields and ocean basins.

We utilize the wide aperture and digital recording capability of SCARLET to collect the large amounts of data required to constrain discrepancies in velocities for these two areas. The data from the northeast Pacific are processed exactly as those from Mexico. We construct T-Δ and p-Δ curves and then model the waveforms with GCA, the spreading center model, as a starting point; the only differences between the final Cascades model and GCA are demanded by the travel time and waveform data. The resolvability of variations between the data sets is tested with a wave field continuation technique modified for spherical earth problems (Clayton & McMechan, 1981; Walck & Clayton, 1984). The high-

quality, dense array data are essential to definitively establish the existence of lateral variations in upper mantle structure between the Gulf of California and the Cascade Range.

Tectonic setting

The study area is one of complex, recent tectonism. We utilize seismic events from northern California around the northeast Pacific Ocean margin to Alaska and the Aleutian trench (see Figure 1a). The earthquakes at distances of more than 30°, as in Paper I, are used for calibrating the array for receiver corrections. These events have rays which bottom under the Pacific plate; their mechanisms are probably thrusts, and they range in depth from shallow to intermediate (the deepest is 123 km; see Table 1). Moving clockwise around the Pacific rim, the next source area is the Queen Charlotte Island fault zone, which moves in a right-lateral sense at 5.5 cm/yr and is the most active fault system in western Canada (Milne et al., 1978; Keen & Hyndman, 1979). Tobin & Sykes (1968), Chandra (1974) and Milne et al. (1978) present fault-plane solutions for earthquakes in this locale which support dextral movement on the Queen Charlotte Island system. The complex Juan de Fuca Ridge system, which separates the Pacific and Juan de Fuca plates, intersects the Queen Charlotte Island fault zone west of Vancouver Island (e. g., Chandra, 1974). Focal mechanisms in this region are indicative of north-south compression with dominantly shallow, strike-slip movement (Rogers, 1979). The actual Juan de Fuca Ridge has few earthquakes, but to the south, the Blanco Fracture Zone and Gorda ridge are very active, with right-lateral strike slip and normal events, respectively. In the

Puget Sound region, most seismicity is shallow, but some events are as deep as 50-60 km (Chandra, 1974); mechanisms are consistent with north-south compression (Crosson, 1972).

Rays from earthquakes closer than 30° turn below the very young oceanic Juan de Fuca plate and also the Cascade Range of Oregon and Washington (Figure 1a). Located along the western coast of the United States, the silicic volcanoes of the Cascades are the result of recent, slow subduction of young oceanic material. Whether or not subduction is continuing at present is the subject of active debate (Crosson, 1972; Riddihough, 1978; Keen & Hyndman, 1979; Heaton & Kanamori, 1983).

Low Pn velocities are typical at the Juan de Fuca Ridge (Shor et al., 1968; Hyndman & Rogers, 1981; Cheung & Clowes, 1981). Davis et al. (1976) observe normal, 8.3 km/s, Pn speeds across the ridge, while Keen & Barrett (1971) present evidence for P-wave anisotropy in this region.

A number of workers have investigated the crustal and uppermost mantle structure of the Pacific Northwest-Vancouver Island region; a complex, laterally varying picture has emerged. Tatel & Tuve (1955) were the first to document the thin (< 20 km) crust in the Oregon Coast Ranges. Their results are substantiated and refined by Dehlinger et al. (1965), Berg et al. (1966) and Johnson & Couch (1970). Dehlinger et al. (1965) and McCollom & Crosson (1975) measure laterally varying Pn velocities for the Cascades region: low values for the western Cascades and higher velocities to the east. Along the Oregon Cascades axis, the crust is thick (44 km), with high crustal velocities and a low Pn velocity value of 7.7 km/s (Leaver et al., 1984).

Near Puget Sound, the uppermost mantle structure includes a high velocity anomaly dipping eastward at about 50° (McKenzie & Julian, 1971; Crosson, 1972). Pn velocities are also low here; 7.8 km/s is a typical value (Crosson, 1972; McCollom & Crosson, 1975; Crosson, 1976).

The crustal structure beneath Vancouver Island is problematic: White & Savage's (1965) refraction study proposes an anomalously thick crust of 50 km for the island. A Pn velocity of 7.8 km/s is observed from body waves (Berry & Forsyth, 1975); this value is consistent with surface wave data as well (Wickens, 1977). Riddihough (1979) points out that the observed gravity data are incongruous with such a great crustal thickness. More recent work by Langston and an associate (Langston, 1977, 1981; Langston & Blum, 1977) and McMechan & Spence (1983) proposes a zone of negative velocity gradient at 40-50 km depth for the entire region. Such a low-velocity zone filled with rocks of lithospheric density (Riddihough, 1979) would explain both the seismic and gravity data.

The complicated, laterally varying shallow structure of the northeast Pacific margin raises questions concerning the nature of the deeper structure under the subducted plate. In the next section we present data pertinent to this problem and attempt to characterize the upper mantle structure in terms of a comparison to the Gulf of California.

The data set

Records of 22 events at distances of 6° to 42° from southern California comprise the data for study of the upper mantle in the Pacific Northwest (Table 1). In Figure 1a, the epicenters of these events are shown, along with 2° arcs

drawn about the midpoints of the appropriate great circle paths. The Mexican data presented in Paper I have a narrow azimuthal range (Figure 1b); the experimental geometry for these northern events is not as favorable. The eight calibration earthquakes from Alaska and the Aleutian trench are at a slightly different azimuth from the 14 events closer than 30°, and their rays turn under the Pacific plate rather than below the Juan de Fuca plate or the continent. The total azimuthal range for the data is 70°. The nearer earthquakes are shallow, with reported depths ranging from 10-32 km. Body wave magnitudes vary from 4.8 to 6.4. These events occurred between September, 1977 and March, 1980 and were recorded by an average of 117 stations at SCARLET with the digital, triggered CEDAR system (Johnson, 1979). Approximately 40 records from each earthquake are included in the final data analysis.

The 22 events yield 853 seismograms covering a 36° range in a rather uneven fashion. While there is an abundance of data from 6.5° to 13°, we have few records from 13° to 16°, and those data are relatively poor in quality. The active seismic zone west of Vancouver Island generates large amounts of high-quality data recorded at distances of 16° to 22°. Figure 2 contains two examples of waveforms from events in this distance range. The relative quiescence of the Queen Charlotte-Fairweather fault system for $M \geq 5$ events during the experimental time period results in poor coverage from 23°-29°, with a large data gap from 26.5° to 29°.

The distribution of seismograms with distance for the northeast Pacific data is quite dissimilar to the Gulf of California data set of Paper I. A record section of 290 seismograms from eight northeast Pacific events (Figure 3) provides an overall view of the northern data. For the Mexican events, we have sparse data

near 18°, which is the most densely sampled range for the northern azimuth. For the Cascade data the poor coverage is farther out at 23°-29°; at those ranges the spreading center has excellent data (compare Figure 4, the southern record section, with Figure 3).

The disparities in seismogram distribution between the two data sets have important implications for the attainable structural resolution for each region. For the Gulf of California, the ample data beyond 20° place tight bounds on structure below 400 km depth and also on the velocity gradient above the 400 km discontinuity, but not on the size and shape of the discontinuity itself. The discontinuous data available beyond 23° from Canadian events do little to constrain the structure of the 660 km discontinuity for that azimuth. Abundant records from 16° to 22°, however, assist in detailed modeling of the 400 km discontinuity below the Cascade Range. Even though these two data sets have their strengths at different ranges, the data overlap sufficiently to compare and contrast the travel times, $dT/d\Delta$ measurements and waveforms and hence the velocity structures of the two regions.

Receiver corrections

To construct station corrections for the northeast Pacific data, we utilize the empirical method outlined in Paper I. Least-squares planes are fit to travel times from eight Alaskan earthquakes ($30° < \Delta < 42°$) (Figure 1a, Table 1) and the residuals averaged to compute corrections. These calibration events define a larger azimuthal swath (30°) than the corresponding Mexican events (8°) and the results are not as consistent. We choose to retain 86 stations with standard deviations of less than 0.15 s as compared to 96 stations and 0.10 s for the

southern data. Our assumption of constant corrections for the entire azimuth band is less certain considering the fanlike (70° azimuthal range) epicenter distribution shown in Figure 1a. As a result, the record alignment obtained after application of the corrections is not as smooth as for the other data set.

We can again compare the empirical corrections to Raikes' (1980) teleseismic P-residuals from the same source area (Figure 5). Despite the lack of adjustments for station elevation and crustal structure in our receiver corrections, the qualitative agreement between the two sets of residuals is striking. Both exhibit early arrivals in a broad east-west zone near 34°N latitude as well as late arrivals in the Imperial Valley, northern Mojave Desert and near the intersection of the Garlock and San Andreas faults.

Travel times

After corrections for ellipticity, earthquake depth and receiver structure, the 22 events generate 1068 usable travel times; 152 of these are secondary arrivals. Figure 6 displays the travel time data, both with and without distance dependent baseline shifts devised to to eliminate the effects of source location and origin time. Superimposed on Figure 6b are travel time curves for two models: GCA'-GCA, the composite spreading center model of Paper I, and CJF, the Cascades-Juan de Fuca model described below.

Close inspection of the two sets of travel time data reveals systematic regional disparities in $T(\Delta)$. Waves from earthquakes offshore northern California and Oregon arrive earlier than the corresponding events in the Gulf of California for distances up to 12°. This discrepancy is not surprising, since the northern travel path is beneath the western margin of the continent instead of

an actively spreading ridge. First arrival times in the range 15°-23° are similar for both groups within the data scatter, but the time separation of the AB and CD branches at 16° is significantly greater for the Vancouver Island events.

The nature of the observable secondary arrivals in the 18°-23° distance range (Figure 6), however, is quite different from the Mexico data. The data described in Paper I do not contain identifiable arrivals from the AB travel time branch past 20° and exhibit strong phases representing the EF branch (reflection from the 660 km discontinuity) from 20° to 24°. Only a few times from one event north of Vancouver Island can be identified as part of the EF branch, in contrast, a number of observations of the AB, or back branch of the 400 km discontinuity, are seen to at least 21° with dubious arrivals extending to 23°. The predominance in the northeast Pacific records of the AB branch over the EF arrivals at these distances signifies a real, quantifiable change in structure between the spreading center and the Cascade Range region at depth.

Due to relatively poor data from 23°-26° and none at all from 26°-29°, we cannot make observations of the back branch (CD) of the 660 km discontinuity for the northern model area. First arrivals beyond 25° are clearly earlier from Alaska than from Central America.

Ray parameter measurements

We obtain 40 estimates of $p(\Delta)$ for the northeast Pacific utilizing the standard processing discussed in Paper I (Table 2); nine of these measurements are for secondary phases. A number of events are too close to SCARLET for the plane wave assumption to be valid, and the least-squares routine yields unreliable results. For these earthquakes, graphical estimates of $dT/d\Delta$ are made

(Table 2). The ray parameter values for these events are only approximate and are more uncertain than the plane-fit estimates for the more distant events.

The data and corresponding curves for CJF and GCA are presented in Figure 7. The above-discussed data distribution with distance is also reflected in the p-Δ measurements. While we can calculate only a single $dT/d\Delta$ value for the forward (EF) branch of the 660 km discontinuity, several estimates are available for the back (AB) branch of the 400 km velocity break. Unfortunately, these measurements are quite scattered, probably due to complex source functions for several events which make accurate picking of secondary phases problematic.

In general, the $p(\Delta)$ data for the northern azimuth are more scattered than the equivalent spreading center values, precluding unambiguous interpretations of lateral variations based on $dT/d\Delta$ data alone. Clear distinctions between the two data groups exist only for first arrivals closer than 17° and the AB secondary phases near 21°. The p-Δ curve for CJF fits these two subsets of the data better than GCA, but in an overall sense $p(\Delta)$ for GCA and CJF (Figure 7) are quite similar. We do not rely heavily on the ray parameter data to make distinctions between the two, but will instead explore relative amplitude differences with waveform modeling, and attempt to compare each entire data set at once using wave field continuation.

Relative amplitude patterns

The seismograms from 6° to 13° are extremely complicated, often high-frequency (relative to 1 Hz) and contain no identifiable, consistent later phases in the P-wave train. While we do not observe reflections from the 400 km discontinuity in this distance range; the one event located 13°-15° from SCARLET is particularly poor and we cannot definitely state that CD arrivals from the 400 km discontinuity do not appear at these distances because of the messy records. In contrast, excellent secondary arrival data exist at 13°-15° for the southern data from an earthquake on the Rivera Fracture Zone (see Figure 13 for a subset of these data).

Beginning at 16°, larger events from the Vancouver Island region provide more useful waveform data. Although the source signatures are often complex, the relative amplitude observations are stable for 16°-22°. At 16°, the first arrival is extremely weak and is followed by a strong reflection from the 400 km discontinuity about 5 s later (Figures 2, 8a). The time separation decreases with increasing distance and waveform complexity (Figure 8b) until the AB-CD cross-over occurs at 18.4°. By a distance of 20°, the AB branch arrives 3 s after the first wave (Figure 8c), and is at least as large as the refracted arrival. It is difficult to determine the exact cutoff distance for the AB branch due to the complicated P-wave codas; a good estimate is 22°-23° (Figure 8d). We see no evidence for a reflection from the 660 km discontinuity at 20° in any of five available record sections. This pattern is in contrast to the southern data for this distance range. At 16°, the ridge data have a weak first arrival, but the strong second phase is only 3 s behind the first, and the crossover point occurs closer to 18°, although there is a gap in the data precisely at that point. Middle

America Trench events at distances of 20° or more feature no AB arrival at all and a strong EF reflection from the 660 km discontinuity starting at 19°.

First arrivals from the northern azimuth are reasonably strong from 20° to 21.5°, then start to weaken relative to the arrival from the 650 km discontinuity (Figure 8e) which is observed for only one event (No. 9 in Table 1) at distances of 21.8° to 23°. Beyond 23°, we cannot identify any obvious secondary arrivals in the northern data, possibly due to poor data quality (23°-26°) or a total absence of records (26°-29°).

These new relative amplitude patterns are similar to those observed for the Gulf of California except in the critical distance range of 18°-23°, where the northeast Pacific records are dominated by the back branch arrival from the 400 km discontinuity and the Mexico data shows mainly the forward branch of the 660 km discontinuity. In the next section, we model the Cascade Range data set using synthetic seismograms and compare the result to GCA and the spreading center data.

Model description

Model CJF (Figure 9, Table 3) satisfies the data described above: travel times, apparent velocities and waveforms. Because we used GCA as the starting point in the modeling process, it is shown along with CJF for comparison. The differences between the two are not drastic but they are significant and resolvable. In essence, CJF is intermediate in character between GCA and previously published models for tectonically active continental regions such as Burdick & Helmberger's (1978) T7 or Burdick's (1981) T9; it features somewhat higher

velocities with a less severe gradient near 200 km and does not coincide with GCA until a depth of 350 km. These results have important implications for the depth extent of lateral heterogeneities in the mantle.

Travel times are dominant in constructing the topmost portion of CJF. The crust and uppermost mantle in the study area is extremely complicated and has large lateral variations in Moho depth and Pn velocity. Figure 10 shows several of the proposed models for shallow structure in the Cascades-Vancouver Island region. Strong variations certainly exist within this oceanic-continental transition zone.

Several refraction studies have established a crust of less than 20 km thickness in the Oregon Coast Range (Tatel & Tuve, 1955; Berg et al., 1966; Shor et al., 1968), but thickening to the east in the Cascades (Dehlinger et al., 1965; Johnson & Couch, 1970; Leaver et al., 1984). The observed Pn velocities correlate with the crustal thickness. Dehlinger et al. (1965) and McCollom & Crosson (1975) document very low values of ≈7.7 km/s west of the Cascades, increasing to about 8 km/s to the east. To further complicate matters, Langston (1977) decides on the basis of converted teleseismic phases that a shallow low velocity zone (to 45 km depth) lies below a 20 km thick upper crust at Corvallis, Oregon.

The anomalous structure at Vancouver Island adds still more complexity to the problem of selecting an appropriate topmost structure for CJF. The absence of Pn first arrivals on a 360 km north-south refraction line led White & Savage (1965) to propose a 50 km, two layer crust for the island. McMechan & Spence (1983) also find a layer of intermediate velocity (≈7.0 km/s) at 15.5 km depth, but agree with Langston (1981) that there might be a shallow low-velocity zone as well, with a total crustal thickness of less than 40 km. Riddihough (1979)

infers crustal sections of 10 km offshore, 20 km beneath the Coast Ranges and 30-40 km farther inland. As an average, we use the Coast Ranges crust of 20 km with the crustal velocity values of Langston (1977). Our Pn velocity of 7.9 km/s is a reasonable average of the widely varying observations for the region. We construct a low-velocity zone that is slightly deeper than Langston's (1981) feature; its 45-80 km depth extent and 7.5 km/s velocity are constrained only by travel times from 8°-15°. The lid thickness and minimum velocity in the low-velocity zone trade off; we choose a lid thickness of 25 km. From 81 to 175 km, CJF's gradient is adjusted to fit first arrival times near 15°. Beyond some simple averaging of available data on local crustal structure, then, the topmost 200 km of CJF are determined from travel time data alone.

The first step in the comparative waveform modeling process is to generate GCA synthetic seismograms for selected data profiles from the northern azimuth. We have already discussed the topmost portion of the final northern model which clearly differs from GCA. Because at least the uppermost 100 km of GCA is not appropriate for the northeast Pacific, waveforms predicted from the southern model are not expected to match the northern data well at short distances. At distances greater than 16°, though, comparisons are useful in determining the changes necessary to fit the Cascade Range data.

In Figure 11, records from an event near Vancouver Island (No. 19 in Table 1) are compared to synthetic profiles for GCA and CJF. The amplitudes, timing and waveshapes for GCA do not match the data throughout the profile. Near 16°, GCA's first arrival (AB branch) is too large and the secondary phase (CD branch) is too small and arrives much too early. Some problems in the relative timing between these two branches could be due to the disparate uppermost mantle

velocities, but close inspection of Figure 11 demonstrates that the entire 400 km discontinuity triplication for GCA occurs too close in distance. The GCA first arrival crossover occurs near 18° instead of the observed 18.4° and at 20°, the AB arrival of GCA (second phase) is both too small and too late. These basic features are confirmed with data from several other events in the same vicinity.

Figure 12 displays the only northern data section which contains any reliable arrivals from the 660 km discontinuity. This event unfortunately exhibits large-amplitude coda arrivals which are problematic to interpret, and the AB branch is difficult to identify near 21°. Even though this record section is not of the same high quality as corresponding data from Mexico, comparisons to GCA are still revealing. Event 9 (Figure 12, Table 1) has weak first arrivals until about 21°, in contrast to GCA. The EF arrival from the lower discontinuity emerges from the noise at about 21.8°, but it is very clear in GCA synthetics as early as 20°. Furthermore, GCA's 660 km reflection is late relative to the first arrivals from 21.8°-23°.

The lack of good waveform data from northeast Pacific events at distances of 23°-28° prevents further assessment of the suitability of GCA's velocities near 660 km depth for the Juan de Fuca region. The differences in first arrival travel times beyond 25° between the two data sets, however, requires slightly faster velocities in the north below 700 km.

Some relatively small adjustments to GCA alter the predicted waveforms so they are much more consistent with the Cascade Range data. After restructuring the top 100 km of CJF as outlined above, we need to increase the absolute velocities from 100-300 km depth to agree with first arrival travel time data from 8°-13°. As in GCA, we have incorporated a region of very slight positive

velocity gradient from 175-250 km to try to reduce the size of the first arriving waves near 16°. This effort is again not totally successful (Figures 11a, c), perhaps due to depth-varying attenuation. A sharp gradient similar to the feature from 225-390 km in GCA exists in CJF, but only deeper than 350 km; this change is in accordance with CJF's higher velocities from 100-300 km and the observation of the AB travel time branch to 22°. In order to increase the time separation between the first arrival and the reflected phase from 16° to 18°, and to shift the crossover point from 18° to 18.4°, the 390 km discontinuity of GCA was placed at 410 km and decreased in size to a 3.8% velocity jump. The effects of these structural changes above 450 km are visible in the CJF synthetic record section computed for a sample event covering 16°-20° (Figure 11c).

An improved fit to the EF branch data near 22° (Figure 12) is achieved by raising the lower discontinuity to 650 km and decreasing the gradient immediately below that velocity jump to make later arrivals less prominent from 20°-21°. A slightly stronger velocity gradient below 700 km matches the faster travel times from Alaskan events from 29°-42°. Figure 3 compares the overall character of the northern data to the CJF synthetics.

While GCA obviously does not satisfy data from Vancouver Island events recorded at Caltech, to establish the validity of the model changes it is vital to demonstrate that CJF is not representative of Gulf of California structure. To do this, we compare synthetic seismogram sections computed with CJF for some of the Mexican events modeled in Paper I. Figure 13 presents data from an earthquake on the Rivera Fracture Zone (No. 2 of Paper I; see Figure 1b for location) recorded at distances of 13° to 17° with both GCA and CJF synthetics plotted below the appropriate traces. CJF does not match these data well. The first

arrival amplitudes are too large for 13°-15° and the reflections from the 410 km discontinuity occur too late for the entire section.

Two southern events in the distance range 18°-23° confirm that CJF is inappropriate in the corresponding 300-700 km depth range. Figure 14 displays the data of event 14 of Paper I, an event inland from the Middle America Trench, with the corresponding synthetic records. For this deeper (96 km) earthquake, the extended AB branch CJF predicts is not compatible with observed seismograms from 18°-20°. CJF's slightly shallower 650 km discontinuity produces secondary arrivals which are too early in the 21°-22° range. The record section and synthetic seismograms for a shallower Mexican event (No. 24 in Paper I) (Figure 15) exhibit the same basic patterns at slightly shifted distances.

The more subtle structural changes near 660 km are reflected in correspondingly smaller changes in CJF synthetic records for 26°-30° (Figure 16). Here the reduced gradient below 650 km in CJF results in a relatively larger first arrival from 26°-28° (these are uncorrected distances for an 80 km deep event) and also small changes in timing. These synthetic waveforms are not as satisfactory as GCA's predictions. The above examples demonstrate that while GCA does not satisfy the data from the north, neither does CJF fit the southern records. The structural differences between the two regions are resolvable and real. The disparities are subtle, however, and may not be noticeable at longer periods. Grand & Helmberger (1984) derive a single model for the entire west coast of North America for long-period shear waves. Both of the study areas discussed here lie within the region of their single model TNA and are presently tectonically active. The greater resolving power of the short-period data assist in defining significant structural variations between the Gulf of California and

the Cascade Range to depths of 350 km.

Wave field continuation comparison

Wave field continuation inversion (Clayton & McMechan, 1981) is useful for comparative structural studies because of its properties: all data are retained in the inversion and the time resolution of the original data transforms directly to depth resolution in the slowness-depth regime, resulting in a realistic measure of model uncertainty. While the original formulation is for flat-earth geometry, this technique adapts readily to spherical earth problems and is well suited for upper mantle studies (Walck & Clayton, 1984).

The inversion consists of two successive linear transformations, the slant stack and downward continuation. Because we work with the entire wave field, not isolated seismograms, dense spatial data sampling is crucial. The slant-stacked data form an image in the ray parameter-intercept time (p,τ) domain (e.g., McMechan & Ottolini, 1980). This image is downward continued with a specified velocity model. Because the continuation requires an input model, the inversion is iterative. Convergence is achieved when the resulting slowness-depth field coincides with the input velocities. Therefore this method is also useful for testing the suitability of existing models for a data set; we can continue the data with any proposed model and check for input-output coincidence. Comparison of different data sets to each other in an objective, global fashion is also easy in the (p, τ) domain. Here we utilize wave field continuation to test CJF's appropriateness for the data set as a whole, to compare the northeast Pacific data with the Gulf of California data, and to test the resolvability of the

differences between GCA and CJF.

We slant stacked and downward continued both the CJF synthetic seismogram section (Figure 4b) and a preprocessed version of the data shown in Figure 4a (Figure 17) to obtain the slant stacks of Figure 18. The data preprocessing comprises three steps: cosine tapering after the first 15 s of signal, a clamped frequency deconvolution to achieve more similar source wavelets, and resampling to a distance interval of 0.1°. We use 70 p values and 1575 τ points, with increments of 0.1 s/deg and 0.08 s, respectively. Also shown in Figure 18 is a stack of a 10-event subset of the Gulf of California data, also preprocessed. The Mexican data are of generally higher quality, as can be seen through comparison of the stacked wave fields; the tau image is much more distinct in Figure 18c than 18b.

Inspection of Figure 18b reveals the strengths and weaknesses of the Cascade Range data set. The large data gap from 26° to 29° causes artifacts to appear in the stack and is responsible for the fuzzy image and low stack amplitudes from 9.3 to 10.7 s/deg, the same region where the synthetic stack (Figure 18a) exhibits high amplitudes. The image is good from 10.7-11.5 s/deg, indicating reliable information about the 410 km discontinuity, but degrades for higher ray parameters because of messy records at close ranges. The stack of the southern data (Figure 18c) is quite different in character. These data produce a clean stack for $p < 11.5$ s/deg, with little information available for higher ray parameters (corresponding to depths shallower than 350 km).

As expected, downward continuation of the deconvolved CJF synthetic data with CJF returns a slowness-depth image equivalent to CJF (Figure 19a). Similarly, continuation of the northern data with CJF yields an image quite

consistent with the input model, although data at higher p are inconclusive (Figure 19b). Continuation of the same data with a smooth velocity distribution containing no discontinuities, such as the Herrin (1968) model (Figure 19c), yields an image that is not coincident with the starting velocities. Thus the Herrin model is not appropriate for these data.

One way of directly comparing two data sets is to continue both groups of data with a single model, quite distinct from the real structure, and see if the two outcomes coincide. Because GCA and CJF are most different above 350 km depth, in slowness-depth space they are disparate mostly for $p > 11.5$ s/deg. Unfortunately, poor data quality at large ray parameter values is evident for both of our data stacks, precluding useful comparison with this approach for these data.

The slant stacks do confirm, however, that the southern data match GCA better than CJF. Because the slant stack of the northern data is poor, we assume that CJF, derived through travel time, $dT/d\Delta$ and synthetic modeling techniques, is appropriate for the northeast Pacific data. Then we compare the stacked southern data to stacked synthetics for both models. Figure 20 presents the same data as in Figure 18c in "reduced τ" format, in which details of curvature and stack amplitude are more obvious. Figures 20c and d are the same stacked data with the minimum loci of GCA and CJF images, respectively, superimposed. The peaks of the stack line up well with the line for GCA (Figure 20c) but are less coincident for CJF (Figure 20d), particularly for ray parameters of 9.2-9.5 s/deg and 12.8-13.0 s/deg. The shift of the lower discontinuity from 660 to 650 km depth causes the shift in peaks near 9 s/deg; the Gulf of California data are consistent with the 660 km depth. The mismatch at higher

values of p is indicative of a different shallow structure beneath the northeast Pacific.

Discussion

At present, the most complete way to obtain a high-resolution view of upper mantle velocity structure is through body-wave modeling constrained with $dT/d\Delta$ and travel time measurements, preferably from a seismic array. This type of analysis is limited to data from regions within 30° of the recording stations unless multiple bounce phases such as PP or SS are utilized.

The easiest way to identify true structural variation is to compare velocity profiles constructed with the same data types and analysis techniques. At SCARLET, the close proximity of two major seismic zones along the eastern Pacific margin facilitates comparative study of the two regions. By analyzing two different groups of seismograms in precisely the same manner, we can describe exactly which features of each data set do not coincide. Earlier workers have successfully compared short-period structure between areas using waveform modeling at regional stations (e.g., Wiggins & Helmberger, 1973; Dey-Sarkar & Wiggins, 1976). Others utilized array-derived travel time and ray parameter estimates but used no relative amplitude constraints (e.g., Ram & Mereu, 1977; Ram et al., 1978; England et al., 1978). With the exception of Rademacher et al. (1983) who employ waveform modeling in study of Greek earthquake data gathered at the 13-station German broadband array GRF, the work presented here is the first to combine the waveform techniques of wave field continuation and synthetic seismogram modeling with traditional array methods in determination of

upper mantle structure.

The two data sets representing the Gulf of California and the Cascade Range underwent identical data processing. Still, several factors contribute to uncertainties in each model. We have attempted to minimize the effects of source mislocations with baseline shifts to the travel time data. These location errors can still have significant effect, however, if a poorly located event is important in the waveform modeling process. Another problem is the assumption of lateral homogeneity along our data "profiles". Tectonic regimes change with distance in both directions from SCARLET. With its wider azimuthal range, the northeast Pacific data are probably more contaminated by lateral heterogeneity effects than the ridge data. We have also ignored the possibility of attenuation variations with depth in the modeling process. Since we cannot uniquely distinguish between effects caused by attenuation and structure, the relationship of the velocities to the Q structure is ambiguous for both data sets. Further, if the attenuation structure varies laterally between the two regions, erroneous interpretations about lateral velocity variations could be made. Finally, SCARLET's teleseismic receiver structure varies with azimuth. The separate sets of empirical station corrections are designed to eliminate receiver structure bias. Since there is a 40° azimuthal difference between the Alaskan calibration events and the Vancouver Island earthquakes, however, the northern corrections (Figure 5) may not be totally appropriate.

When comparing our two data sets and the resultant models, it is important to remember the differences in data quantity, quality and distance distribution between the two record groups. Below the 660 km discontinuity, for example, the gradients of the two models diverge. Many travel time and $dT/d\Delta$

measurements for distances up to 40° as well as waveform modeling from 23°-28° constrain GCA's structure in this depth range. In contrast, CJF's velocities are not well known near the lower discontinuity because of a lack of data from 26°-29°. Waves from northern earthquakes beyond 29°, though, arrive earlier than their southern counterparts, necessitating the steeper velocity gradient for CJF below 700 km.

Closer to the surface, GCA's lower discontinuity is at 660 km and its depth is well constrained, a 10 km upward adjustment to a 650 km discontinuity for CJF is suggested by waveform data near 22°. That CJF's 650 km velocity jump is not compatible with the Mexican data is shown by wave field continuation.

The upper discontinuity lies at 390 km in GCA and 410 km for CJF. At these depths, the more complete northeast Pacific data from 16° to 20° establish the depth to CJF's 410 km discontinuity with more certainty than GCA's 390 velocity break. An unfortunate data gap near 18° for the southern data adds to the uncertainty of the exact depth of GCA's upper discontinuity because the first-arrival crossover point is not observed directly. Relative timing of arrivals from 13°-15° do not pin down the absolute depth to the discontinuity beneath the spreading center; the first arrivals at those distances are very dependent on poorly known shallow structure. Attempts to move the upper discontinuity in GCA to 410 km while retaining the steep velocity gradient above it were not successful. We could not match relative arrival times, absolute arrival times and relative amplitudes simultaneously with the deeper velocity jump.

Both data sets have many records from 20°-23°; the character of the AB branch arrival in this distance range controls the velocity gradient from about 300-400 km, and the first arrivals (CD branch) prescribe the structure in the

transition zone. We do not require any changes from 400-650 km depth: both sets of data have amazingly similar first-arrival travel times. The data do demand a different gradient above 400 km for the Cascade Range. Clear observations of the AB branch to 21° from Vancouver Island events are in direct contrast to null-observations for the south past 19° for nine events. Perhaps because the AB branch cuts off so early, the forward branch (EF) reflection of the 660 km discontinuity is very prominent in the Mexico data as early as 19° (see Figures 14, 15), while it is not seen from the north until nearly 22° (Figure 12). This repeatable contrast between the two groups of data supports GCA's steep gradient from 225-390 km and CJF's less severe rate of increase to 350 km.

Changes between the models above 200 km are largely dictated by the regional uppermost mantle structure and also by the travel times for $\Delta < 15°$. For GCA, velocities must be low to 200 km depth to accommodate the large gradient above the upper discontinuity. Since the gradient in CJF is more moderate, the low-velocity zone and speeds below 100 km are constructed to fit the travel times at close distances. These structures are by no means unique. Better control on velocities at asthenospheric depths would improve the entire velocity profile for each region.

The wave field continuation experiments emphasize the resolution capabilities of each data set as a function of ray parameter. For this technique to be valuable, we need dense, very high-quality data. The method has potential as a basis for model and data set comparison and in quantifying data resolution.

Now that we have documented the changes between CJF and GCA in detail, it is instructive to compare them to a model designed for the entire western

United States, T7 (Burdick & Helmberger, 1978). Figure 21a displays all three velocity profiles, and Figure 21b displays the cumulative one-way vertical travel times of T7, GCA and CJF. The velocity-depth plot reveals that CJF is more similar to T7 than GCA, especially below 200 km. Above that depth, the relatively unconstrained structure varies widely from model to model. CJF is actually intermediate between T7 and GCA between 200 and 350 km, having slightly lower velocities than T7. The one-way travel times illustrates CJF's median character very nicely (Figure 21b). Relative to the Herrin model, all three regional models are similar below 400 km depth. Above 240 km, GCA's slower velocities result in very positive residual values, while CJF's times flatten with respect to Herrin, as do T7's residuals. The various low-velocity zone shapes affect the near-surface cumulative times.

That CJF is intermediate in character between continental and ridge models is not surprising because it represents a transition region between tectonically active continent and very young oceanic material. Dey-Sarkar & Wiggins (1976) model western Canada upper mantle structure, including some data near the continental margin for $\Delta < 22°$. The AB travel time branch for their model WCA extends to 24°, but is constrained only by data sensitive to structure inland, beneath the main continent. Their observations for $\Delta < 20°$ are in good agreement with our records for the Cascade region. Similarly, Burdick & Helmberger (1978) observe the AB branch in the western United States to 24°, but their data are gathered much farther inland than our records.

In the oceanic regime, Ram & Mereu's (1977) work with Indian Ocean data recorded at the Gauribidanur seismic array confirm the analysis of Paper I: they do not observe the AB branch past a distance of 19°. England et al.'s (1978)

oceanic model NAT predicts an AB branch that extends beyond 20°, but the travel paths used for the model vary widely in azimuth and sample regions under much older oceanic lithosphere.

Significant evidence exists for the variation of velocity gradient between 200 and 400 km as a function of tectonic regime. For some shield areas (e.g., King & Calcagnile, 1976) the gradient is very shallow; it is more moderate beneath tectonically active continental areas and older oceanic material (Fukao, 1977; Burdick & Helmberger, 1978; England et al., 1978) and very steep beneath at least one oceanic ridge (Paper I). The transition from a young oceanic plate to a continent, represented by CJF, has structure intermediate to the young ocean and young continent regimes. From 200-350 km the gradient is moderate and from 350-400 km the velocities increase very quickly. On a global scale, results from the assimilation of many different upper models for differing tectonic settings support lateral heterogeneities in the mantle to depths close to the 400 km discontinuity; these heterogeneities are functions of surface tectonic regimes.

Acknowledgments

Don Anderson, Rob Clayton and Steve Grand reviewed the manuscript. Don Helmberger and Jeff Given provided valuable advice during the course of the research. This work was supported by NASA contract NSG-7610 and National Science Foundation grant EAR811-5236. Contribution No. 4067, Division of Geological and Planetary Sciences, California Institute of Technology, Pasadena, CA, 91125.

References

Berg, J. W., L. Trembly, D. A. Emilia, J. R. Hutt, J. M. King, L. T. Long, W. R. McKnight, S. K. Sarmah, R. Souders, J. V. Thiruvathukal & D. A. Vossler, 1966. Crustal refraction profile, Oregon Coast Range, *Bull. Seism. Soc. Am.*, **56**, 1357-1362.

Berry, M. J. & D. A. Forsyth, 1975. Structure of the Canadian Cordillera from seismic refraction and other data, *Can. J. Earth Sci.*, **12**, 182-208.

Burdick, L. J., 1981. A comparison of the upper mantle structure beneath North America and Europe, *J. Geophys. Res.*, **86**, 5926-5936.

Burdick, L. J. & D. V. Helmberger, 1978. The upper mantle P velocity structure of the western United States, *J. Geophys. Res.*, **83**, 1699-1712.

Chandra, U., 1974. Seismicity, earthquake mechanisms and tectonics along the western coast of North America, from 42°N to 61°N, *Bull. Seism. Soc. Am.*, **64**, 1529-1549.

Cheung, H. P. Y. & R. M. Clowes, 1981. Crustal structure from P- and S-wave analyses: ocean bottom seismometer results in the north-east Pacific, *Geophys. J. R. astr. Soc.*, **65**, 47-73.

Clayton, R. W. & G. A. McMechan, 1981. Inversion of refraction data by wave field continuation, *Geophysics*, **46**, 860-868.

Crosson, R. S., 1972. Small earthquakes, structure, and tectonics of the Puget Sound region, *Bull. Seism. Soc. Am.*, **62**, 1133-1171.

Crosson, R. S., 1976. Crustal structure modeling of earthquake data 2. Velocity structure of the Puget Sound region, Washington, *J. Geophys. Res.*, **81**, 3047-3054.

Davis, E. E., C. R. B. Lister & B. T. R. Lewis, 1976. Seismic structure of the Juan de Fuca Ridge: ocean bottom seismometer results from the median valley, *J. Geophys. Res.*, **81**, 3541-3555.

Dehlinger, P., E. F. Chiburis & M. M. Collver, 1965. Local travel-time curves and their geologic implications for the Pacific Northwest states, *Bull. Seism. Soc. Am.*, **55**, 587-607.

Dey-Sarkar, S. K. & R. A. Wiggins, 1976. Upper mantle structure in western Canada, *J. Geophys. Res.*, **81**, 3619-3632.

England, P. C., B. L. N. Kennett & M. H. Worthington, 1978. A comparison of upper-mantle structure beneath Eurasia and the north Atlantic and Arctic Oceans, *Geophys. J. R. astr. Soc.*, **54**, 575-585.

Grand, S. & D. Helmberger, 1984. Upper mantle shear velocity structure of North America, *Geophys. J. R. astr. Soc.*, **76**, 399-438.

Heaton, T. H. & H. Kanamori, 1983. Seismic potential associated with subduction in the northwestern United States, submitted to Bulletin of the Seismological Society of America.

Herrin, E., 1968. 1968 seismological tables for P phases, *Bull. Seism. Soc. Am.*, **58**, 1193-1241.

Hyndman, R. D. & G. C. Rogers, 1981. Seismicity surveys with ocean bottom seismographs off western Canada, *J. Geophys. Res.*, **86**, 3867-3880.

Johnson, C. E., 1979. Part I: CEDAR - An approach to the computer automation of short-period local seismic networks, Part II, Seismotectonics of the Imperial Valley of southern California, Ph.D. thesis, Calif. Inst. of Technol., Pasadena, 332 pp.

Johnson, L. R., 1967. Array measurements of P velocities in the upper mantle, *J. Geophys. Res.*, **72**, 6309-6325.

Johnson, S. H. & R. W. Couch, 1970. Crustal structure in the north Cascade mountains of Washington and British Columbia from seismic refraction measurements, *Bull. Seism. Soc. Am.*, **60**, 1259-1269.

Keen, C. E. & D. L. Barrett, 1971. A measurement of seismic anisotropy in the northeast Pacific, *Can. J. Earth Sci.*, **8**, 1056-1064.

Keen, C. E. & R. D. Hyndman, 1979. Geophysical review of the continental margins of eastern and western Canada, *Can. J. Earth Sci.*, **16**, 712-747.

King, D. W. & G. Calcagnile, 1976. P-wave velocities in the upper mantle beneath Fennoscandia and western Russia, *Geophys. J. R. astr. Soc.*, **46**, 407-432.

Langston C. A., 1977. Corvallis, Oregon, crustal and upper mantle receiver structure from teleseismic P and S waves, *Bull. Seism. Soc. Am.*, **67**, 713-724.

Langston, C. A., 1981. Evidence for subducting lithosphere under southern Vancouver Island and western Oregon from teleseismic P wave conversions, *J. Geophys. Res.*, **86**, 3857-3866.

Langston, C. A. & D. E. Blum, 1977. The April 29, 1965 Puget Sound earthquake and the crustal and upper mantle structure of western Washington, *Bull. Seism. Soc. Am.*, **67**, 693-711.

Leaver, D. S., W. D. Mooney & W. M. Kohler, 1984. A seismic refraction study of the Oregon Cascades, *J. Geophys. Res.*, in press.

McCollom, R. L. & R. S. Crosson, 1975. An array study of upper mantle velocity in Washington state, *Bull. Seism Soc. Am.*, **65**, 467-482.

McKenzie, D. & B. Julian, 1971. Puget Sound, Washington earthquake and the mantle structure beneath the northwestern United States, *Bull. Geol. Soc. Am.*, **82**, 3519-3524.

McMechan, G. A. & R. Ottolini, 1980. Direct observation of a p - τ curve in a slant stacked wave field, *Bull. Seism. Soc. Am.*, **70** 775-789.

McMechan, G. A. & G. D. Spence, 1983. P-wave velocity structure of the Earth's crust beneath Vancouver Island, *Can. J. Earth Sci.*, **20**, 742-752.

Milne, W. G., G. C. Rogers, R. P. Riddihough, G. A. McMechan & R. D. Hyndman, 1978. Seismicity of western Canada, *Can. J. Earth Sci.*, **15**, 1170-1193.

Niazi, M. & D. L. Anderson, 1965. Upper mantle structure of western North America from apparent velocities of P waves, *J. Geophys. Res.*, **70**, 4633-4640.

Rademacher, H., R. I. Odom & R. Kind, 1983. The upper mantle structure under south-east Europe derived from GRF broadband records of Greek earthquakes, *J. Geophys.*, **52**, 7-13.

Raikes, S. A., 1978. Part I: Regional variations in upper mantle compressional velocities beneath southern California, Part II, Post shock temperatures: their experimental determination, calculation, and implications, Ph. D. thesis, Calif. Inst. of Technol., Pasadena, 307 pp.

Raikes, S. A., 1980. Regional variations in upper mantle structure beneath southern California, *Geophys. J. R. astr. Soc.*, **63**, 187-216.

Ram, A. & R. F. Mereu, 1977. Lateral variations in upper mantle structure around India as obtained from Gauribidanur seismic array data, *Geophys. J. R. astr. Soc.*, **49**, 87-113.

Ram, A., R. F. Mereu & D. H. Weichert, 1978. The identification and interpretation of upper mantle travel-time branches from measurements of dT/dΔ made on data recorded at the Yellowknife seismic array, *Can. J. Earth Sci.* , **15** , 227-236.

Riddihough, R. P., 1978. The Juan de Fuca plate, *EOS Trans. AGU*, **59** , 836-842.

Riddihough, R. P., 1979. Gravity and structure of an active margin -- British Columbia and Washington, *Can. J. Earth Sci.*, **16** , 350-363.

Rogers, G. C., 1979. Earthquake fault plane solutions near Vancouver Island, *Can. J. Earth Sci.*, **16** , 523-531.

Shor, G. G., P. Dehlinger, H. K. Kirk & W. S. French, 1968. Seismic refraction studies off Oregon and northern California, *J. Geophys. Res.*, **73** , 2175-2194.

Tatel, H. E. & M. A. Tuve, 1955. Seismic exploration of a continental crust, *Geol. Soc. Am. Sp. Pap.* **62** , 35-50.

Tobin, D. G. & L. R. Sykes, 1968. Seismicity and tectonics of the northeast Pacific Ocean, *J. Geophys. Res.*, **73** , 3821-3845.

Walck, M. C., 1984. The P-wave upper mantle structure beneath an active spreading center: the Gulf of California, *Geophys. J. R. astr. Soc.*, in press.

Walck, M. C. & R. W. Clayton, 1984. Wave field continuation of upper mantle P waves, submitted to Bulletin of the Seismological Society of America.

White, W. R. H. & J. C. Savage, 1965. A seismic refraction and gravity study of the Earth's crust in British Columbia, *Bull. Seism. Soc. Am.*, **55** , 463-486.

Wickens, A. J., 1977. The upper mantle of southern British Colombia, *Can. J. Earth Sci.*, **14** , 1100-1115.

Wiggins, R. A. & D. V. Helmberger, 1973. Upper mantle structure of the western United States, *J. Geophys. Res.*, **78**, 1870-1880.

Figure Captions

Figure 1. a) Locations of the 22 earthquakes used in this paper. Dots show the epicenters of the eight calibration events; stars denote the 14 events closer than 30°. The short lines are 2° arcs drawn around the midpoints of the great circle paths to Pasadena for all events. Notice that the calibration events bottom beneath the Pacific Ocean, while for the other events, rays turn near the continental margin. b) Same information for the 29 events from Paper I. Notice the narrower azimuthal distribution of events.

Figure 2. Record sections for two events near Vancouver Island. a) Event 19 in Table 1. A weak first phase is followed by the strong reflection from the 400 km discontinuity from 16°-18°. Past 19°, the AB branch is now a secondary arrival moving out with distance. It is still very strong at 20°. b) Event 8 in Table 1. The same general patterns are visible.

Figure 3. a) Composite record section of 290 seismograms from eight events spanning 9°-39.5°. Inclusion of all available records does not eliminate the gaps in the data seen here. Records are corrected for event depth and receiver structure and are low-pass filtered with a 5 Hz high frequency roll off. Each trace has the same maximum amplitude. b) Synthetic record section made with model CJF (Table 3); 301 seismograms are shown.

Figure 4. a) Data record section of 10 events representing Gulf of California upper mantle structure. The section spans 9°-40°; 373 records are shown. b)

GCA synthetic record section on the same scale. Source wavelets vary with distance. Again 301 seismograms comprise the section.

Figure 5. a) Empirical station corrections in contour format. These values include the effects of station elevation and shallow structure. Note the wide, east-west band of negative values near 34° latitude becoming more positive to the north and south. b) P residuals of the same source area relative to station GSC (Raikes, 1978). Adjustments for elevation, sediments and Moho variation have been made. The same pattern is observed; much more negative residuals are found just north of the Salton Sea with more positive delays both south and north. The contour interval is 0.25 s.

Figure 6. Reduced travel time data. a) The 1068 times (152 secondary arrivals) are plotted with only depth and receiver corrections applied. Note the large scatter for $\Delta < 15°$. b) The same data after distance-varying baseline shifts are applied. The model derived from these data, CJF (see Table 3, Figure 9), is superimposed along with the Gulf of California model (see (c)). Notice that GCA'-GCA is too slow for $\Delta < 12°$, $14° < \Delta < 18°$ and $\Delta > 30°$. c) Models GCA' and GCA. The combined model GCA'-GCA consists of GCA' for the top 150 km underlain by GCA. GCA' represents the axial region of the Gulf of California while GCA is more appropriate for adjacent continental areas.

Figure 7. Ray parameter measurements for the northeast Pacific data, displayed with the corresponding curves for both CJF and GCA. These data are not very useful in distinguishing between the two models but are generally more

consistent with CJF.

Figure 8. Relative amplitude patterns for the northern data. a) Near 16°, the first arrival (AB branch) is very weak, while the reflection from the 400 km discontinuity is quite strong. b) At 18° the CD branch has moved in closer to the first arrival but not yet crossed it. c) At 20°, the arrow indicates the approximate onset of the AB branch, now a large secondary phase. d) The larger phase 5 s behind the first break on this noisy record may be the AB arrival, still comparable in size to the CD branch at 21°. e) The record at 23° shows the reflection from the 650 km discontinuity 2 s behind the first-arriving CD branch. This relatively poor-quality record is typical of observations in this distance range from Queen Charlotte Island Fault events.

Figure 9. Models CJF and GCA. CJF is derived for the Cascade Ranges data set using GCA (Paper I) as a starting model. The important differences between the two are in the absolute velocities and gradients above 400 km; also, CJF's velocities are higher below 800 km.

Figure 10. Comparison of five crustal models for the northwest United States-Vancouver Island region. There is little agreement between the studies.

Figure 11. Observed and synthetic record sections for event 19 of Table 1. a) Data. Only a subset of the usable data are shown. b) GCA synthetics. From 16°-18° the first arrival is too large and the second phase too early. Past 19°, the second arrival (AB branch) is too late and decays in amplitude too quickly,

indicating that GCA's large gradient above 390 km is too severe for the northern data. c) CJF synthetics. Relative amplitudes and timing are better than GCA at all distances.

Figure 12. Data and synthetic sections for event 9 (Table 1). a) Data. This earthquake has large-amplitude arrivals 8-9 s after the first arrival; the first 5-7 s are important for the modeling. First arrivals are weak from 19°-20°; the AB branch is not obvious in this distance range. Initial phases are stronger past 21°. Near 22°, the reflection from the 650 km discontinuity (EF branch) is visible as a second arrival. b) GCA synthetic section. Before 22°, the first arrival and the EF branch are both too strong. The 650 km reflection is a little late at all observed distances. c) CJF synthetic section. The first-arrival relative amplitudes are correct. CJF's slightly shallower 650 km discontinuity matches the data better from 22°-23°.

Figure 13. Comparison of GCA and CJF for Gulf of California data from 13°-17° (event 2 of Paper I). For each set of three traces, the data is topmost, GCA is in the middle and CJF is plotted lowest. The reflection from CJF's 410 km discontinuity arrives much too late at all distances. CJF's first-arrival amplitude is also much too large. GCA's relative amplitudes and timing match the data better.

Figure 14. GCA and CJF compared to Mexican event 14 (Paper I). The distances shown here are not corrected for the event depth of 96 km. See Figure 13 for format explanation. From 18.5°-19.5°, CJF predicts a very large AB arrival that

is not in the data, while GCA's sharp gradient above 390 km cuts off that branch before 19° for this event depth. Beyond 20°, CJF's slightly shallower 650 km discontinuity results in small timing errors.

Figure 15. GCA and CJF compared to Mexican event 24 (Paper I). This earthquakes' depth is 52 km; distances are not corrected. See Figure 13 for format. As in Figure 14, we see that the large AB branch produced by CJF up to 20.5° is not present in the data. CJF's more moderate gradient above 350 km is not sufficient for the southern data set.

Figure 16. GCA and CJF compared to the 80 km deep event 27 of Paper I. As before, distances are uncorrected for source depth; see Figure 13 for format. Due to the smaller differences between GCA and CJF below 450 km, the synthetics for the two models are similar from 25°-30°. For this distance range, the model differences are constrained by travel times, not these subtle waveform variations. GCA's amplitude ratios from 25°-27° do fit this record section better.

Figure 17. Northeast Pacific preprocessed record section. Nine events from 7° to 42° have been cosine tapered, deconvolved, and resampled to a 0.1° distance interval; there are 269 seismograms. Notice that the overall data quality is poorer than that of the southern data (Figure 4).

Figure 18. Slant stacks. a) CJF deconvolved synthetics. b) Northeast Pacific processed data. Note the linear artifacts at high ray parameters. c) gulf of

California processed data. The image is much clearer for lower p than in (b). The stack loses power for $p > 11.5$ s/deg.

Figure 19. Downward continued data. a) CJF synthetics continued with CJF. The model and "data" agree. A plotting artifact makes the model line appear lower than the image. b) Northern data continued with CJF. The agreement is satisfactory. c) Northern data continued with the Herrin (1968) velocities. Notice that the image falls consistently below the line; the Herrin model is not appropriate for these data.

Figure 20. Reduced τ slant stacks. These (p,τ) diagrams have been replotted relative to an arbitrary line: $\tau = -21.667\ p + 130$. a) Gulf of California data. b) GCA synthetics. A line drawn at the onset of the image. c) Gulf of California data with the line of part b superimposed. The data and synthetics match well. d) Gulf of California data with a similar line for the CJF' synthetic stack superimposed. The agreement is not as good, particularly from 9.4-9.8 s/deg and 12.7-13.0 s/deg. The differences are subtle, however.

Figure 21. a) Comparison of CJF, GCA and T7 (Burdick & Helmberger, 1978). Between 200 and 350 km depth, CJF's velocity gradient is similar to T7's but the absolute velocities are lower. b) Cumulative one-way vertical travel times for these three models.

Table 1
Epicentral Information

Event No.	Date Day	Mo.	Year	Origin Time Hr.	Min.	S.	Lat. deg.	Long. deg.	Depth km	Mag. m_b
1	19	Jul.	1978	09	32	08.6	56 46.14	-151 38.82	33.	5.7
2	25	May	1979	16	45	27.3	52 36.66	-167 01.14	23.	6.0
3	12	Apr.	1978	03	42	03.5	56 25.38	-152 41.46	14.	6.0
4	01	Sep.	1979	05	27	17.6	53 58.68	-165 12.24	69.	5.8
5	24	Mar.	1980	03	59	51.3	52 58.14	-167 40.20	33.	6.2
6	20	May	1979	08	14	00.1	56 38.82	-156 43.50	71.	6.4
7	17	Aug.	1978	18	52	28.4	59 53.10	-153 31.92	123.	5.7
8	02	Jun.	1978	20	41	43.7	50 15.54	-127 41.28	21.	5.1
9	11	Jul.	1978	02	55	01.6	52 45.90	-132 06.24	10.	5.4
10	13	Mar.	1979	12	00	17.2	49 59.22	-129 41.28	10.	5.4
11	21	Jun.	1979	17	03	17.5	51 19.38	-130 18.90	10.	5.0
12	11	Jul.	1979	12	28	02.9	55 19.38	-134 57.90	10.	5.1
13	14	Mar.	1979	15	13	32.4	50 06.48	-129 42.96	10.	5.3
14	28	Feb.	1979	21	27	06.1	60 38.52	-141 35.58	10.	6.4
15	03	Feb.	1979	09	58	16.1	40 53.40	-124 24.78	28.	5.2
16	07	Apr.	1979	06	18	33.0	41 59.22	-126 48.96	15.	5.5
17	01	Aug.	1979	10	50	26.6	41 01.86	-127 13.26	15.	5.3
18	03	Mar.	1980	14	17	04.6	40 36.00	-125 01.98	5.	5.0
19	25	Jul.	1978	23	30	50.9	50 18.18	-127 34.62	11	5.3
20	28	Jul.	1977	15	22	18.5	44 14.64	-128 57.72	15.	5.1
21	06	Oct.	1978	21	26	31.8	40 27.12	-124 35.22	32.	4.8
22*	13	Feb.	1979	05	34	25.9	55 27.18	-157 09.72	33.	5.9

*This event is used only for the receiver corrections of Figure 5.
Source: U. S. Geological Survey P. D. E. Monthly Listings

Table 2

dT/dΔ Data

Event No.	Δ deg.	p s/deg.	RMS Error, s	Arrival Type	No. of Stations
1	33.096	8.71	.088	F	48
2	39.909	8.22	.096	F	52
3	33.024	8.71	.073	F	30
4	39.175	8.24	.061	F	68
5	40.318	8.15	.081	F	59
6	35.461	8.53	.060	F	78
7	35.703	8.52	.096	F	50
8	17.450	12.57	.422	F	20
	19.084	10.51	.099	F	9
	17.485	10.92	.480	L	19
9	21.406	10.40	.266	F	30
	20.922	12.51	.427	L	26
	22.449	9.56	.266	L	11
10	17.424	11.99	.346	F	20
	19.317	10.49	.256	F	21
	17.381	10.90	.388	L	19
	19.569	11.52	.370	L	12
11	19.812	10.97	.386	F	45
	20.127	12.16	.303	L	36
12	24.685	9.16	.265	F	23
13	19.412	10.98	.323	F	19
	19.468	11.48	.283	L	19
14	30.094	8.98	.180	F	25
	31.852	8.72	.164	F	30
15	8.007	12.68	**	F	8
	10.152	13.42	**	F	12
16	10.563	13.94	**	F	13
	12.690	13.63	**	F	7
17	9.226	14.23	**	F	12
	11.438	13.28	**	F	9
18	7.203	14.68	**	F	9
	9.435	13.95	**	F	13
19	17.422	12.48	.500	F	23
	19.125	10.54	.240	F	19
	17.392	11.10	.420	L	22
	19.283	11.91	.365	L	12
20	13.308	12.95	**	F	10
	15.512	12.74	.189	F	9
21	9.693	13.42	**	F	10
22	35.062	8.57	.077	F	57

** For these events, dT/dΔ is calculated graphically.
F denotes first arrivals, L later phases.

Table 3

Model CJF

Depth km	Velocity km/s	Depth km	Velocity km/s
0.	5.500	275.	8.400
10.	5.500	300.	8.475
11.	6.700	325.	8.560
19.	6.700	350.	8.660
20.	7.900	375.	8.760
45.	7.900	400.	8.860
46.	7.500	410.	8.900
80.	7.500	411.	9.250
81.	7.900	450.	9.476
100.	7.952	538.	9.800
125.	8.025	620.	10.060
150.	8.100	650.	10.360
175.	8.175	651.	10.650
200.	8.225	700.	10.750
225.	8.275	800.	11.100
250.	8.325	970.	11.400

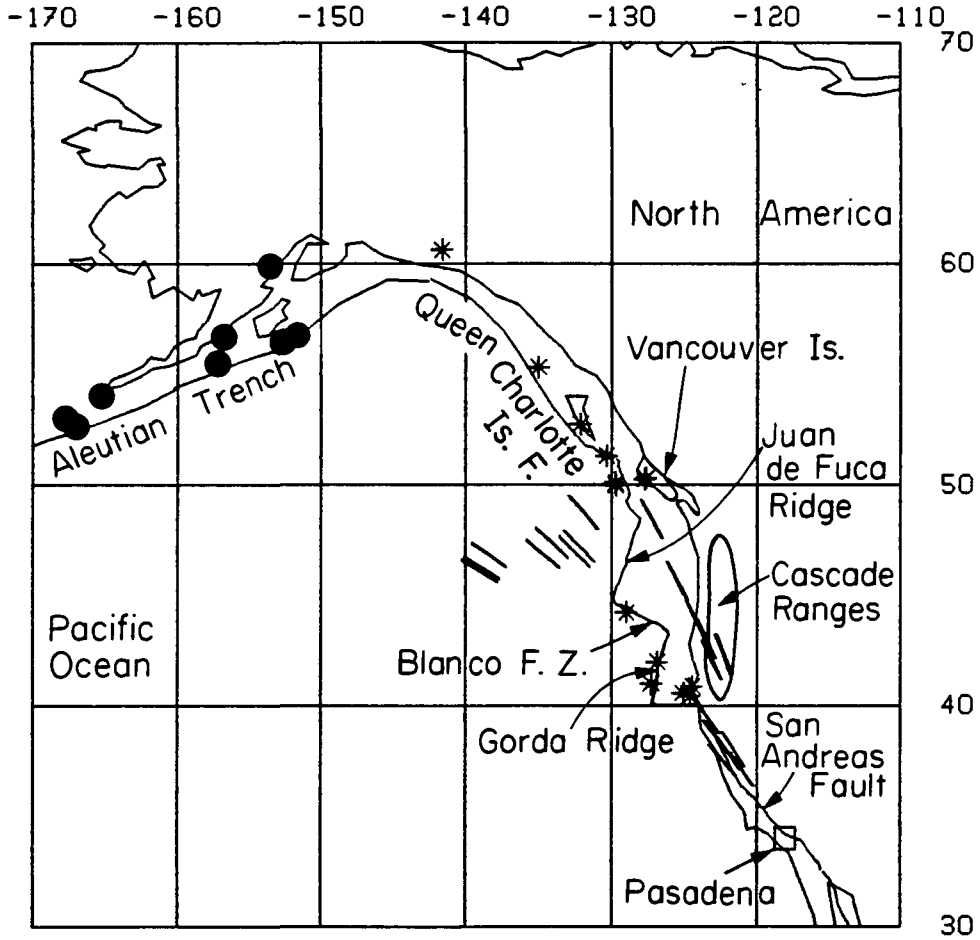
-170
-160
-150
-140
-130
-120
-110
70
60
50
40
30
North America
Vancouver Is.
Juan de Fuca Ridge
Cascade Ranges
Queen Charlotte Is. F.
Aleutian Trench
Pacific Ocean
Blanco F. Z.
Gorda Ridge
San Andreas Fault
Pasadena

Figure 1a

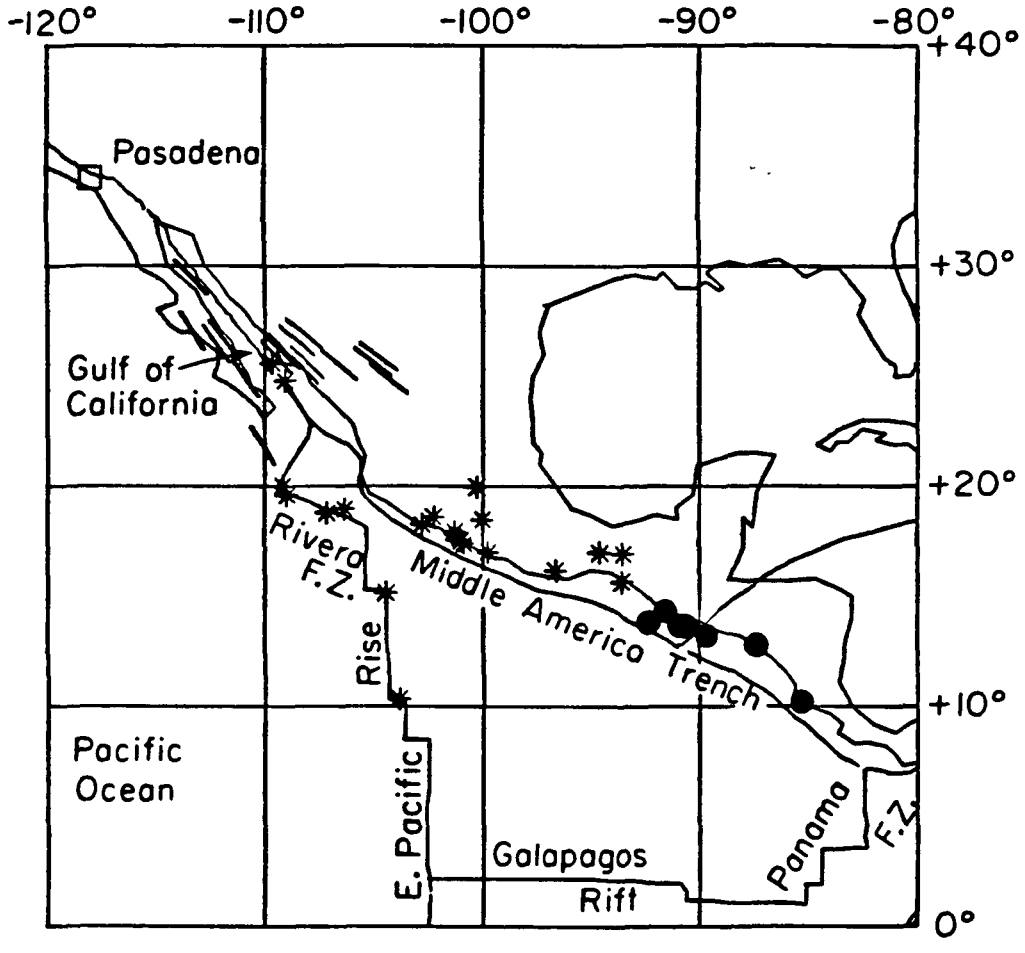
-120°
-110°
-100°
-90°
-80°
+40°
+30°
+20°
+10°
0°
Posadena
Gulf of California
Rivera F.Z.
Rise
Middle America Trench
Pacific Ocean
E. Pacific
Galapagos Rift
Panama F.Z.

Figure 16

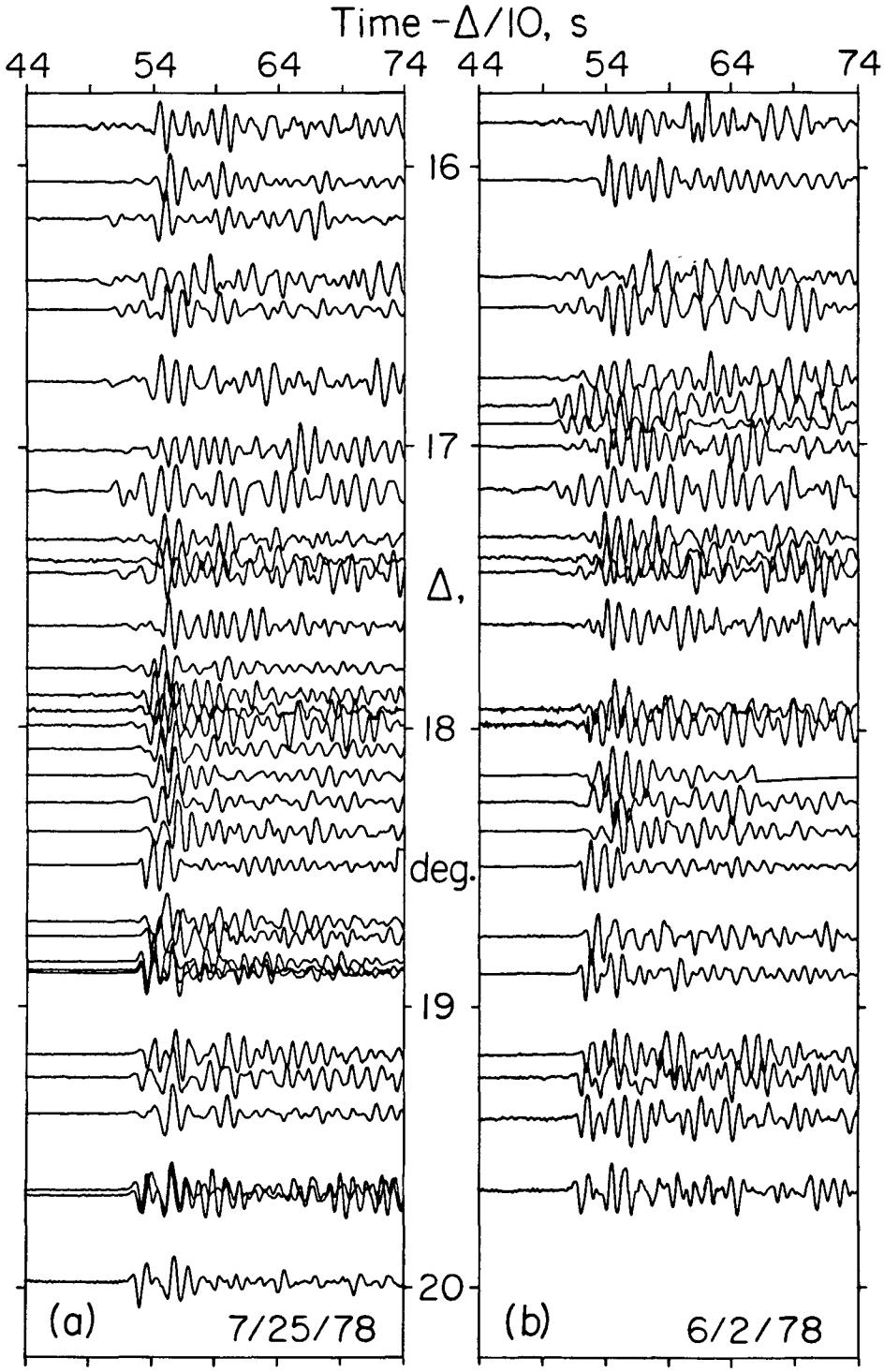

Figure 2

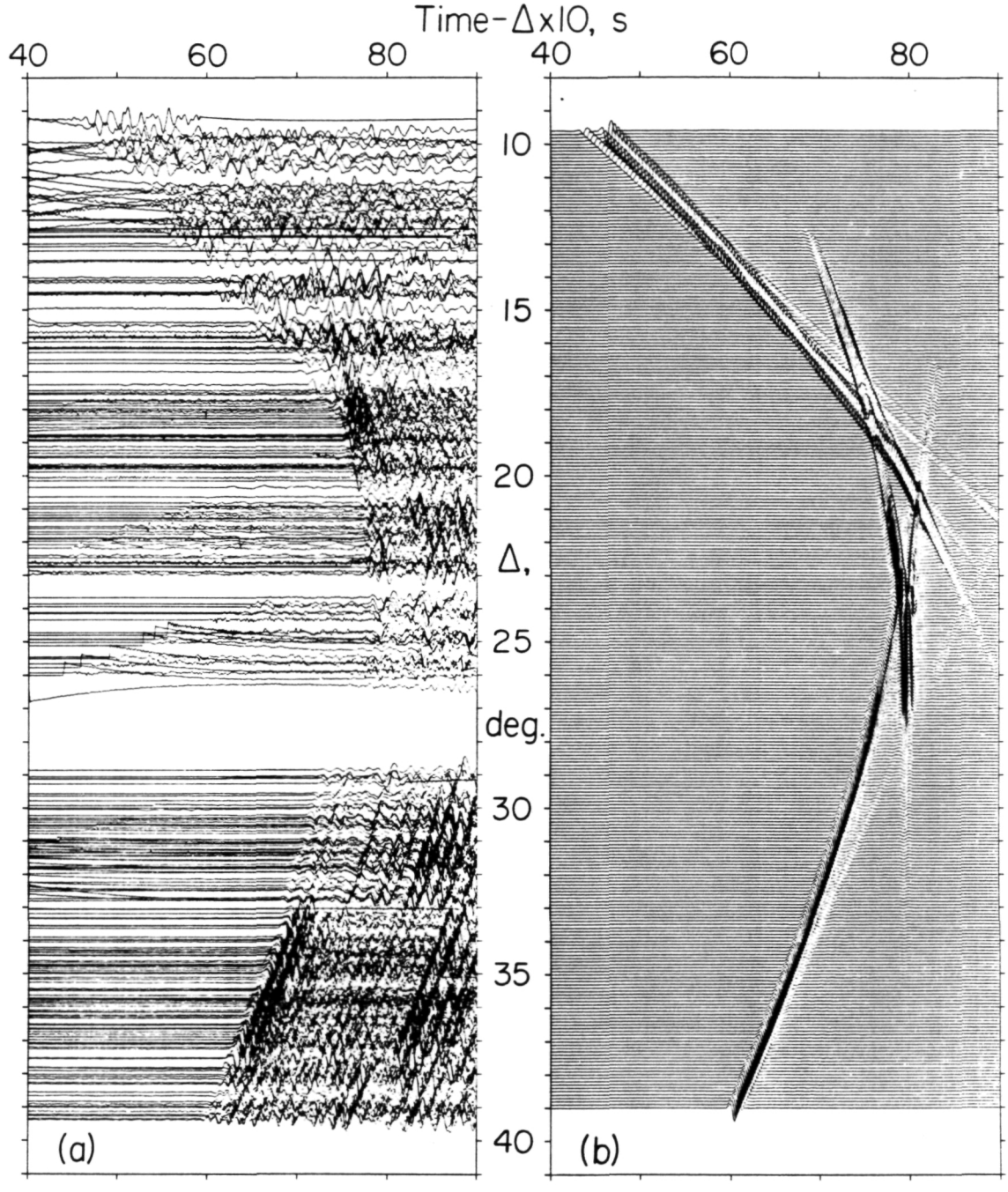

Figure 3

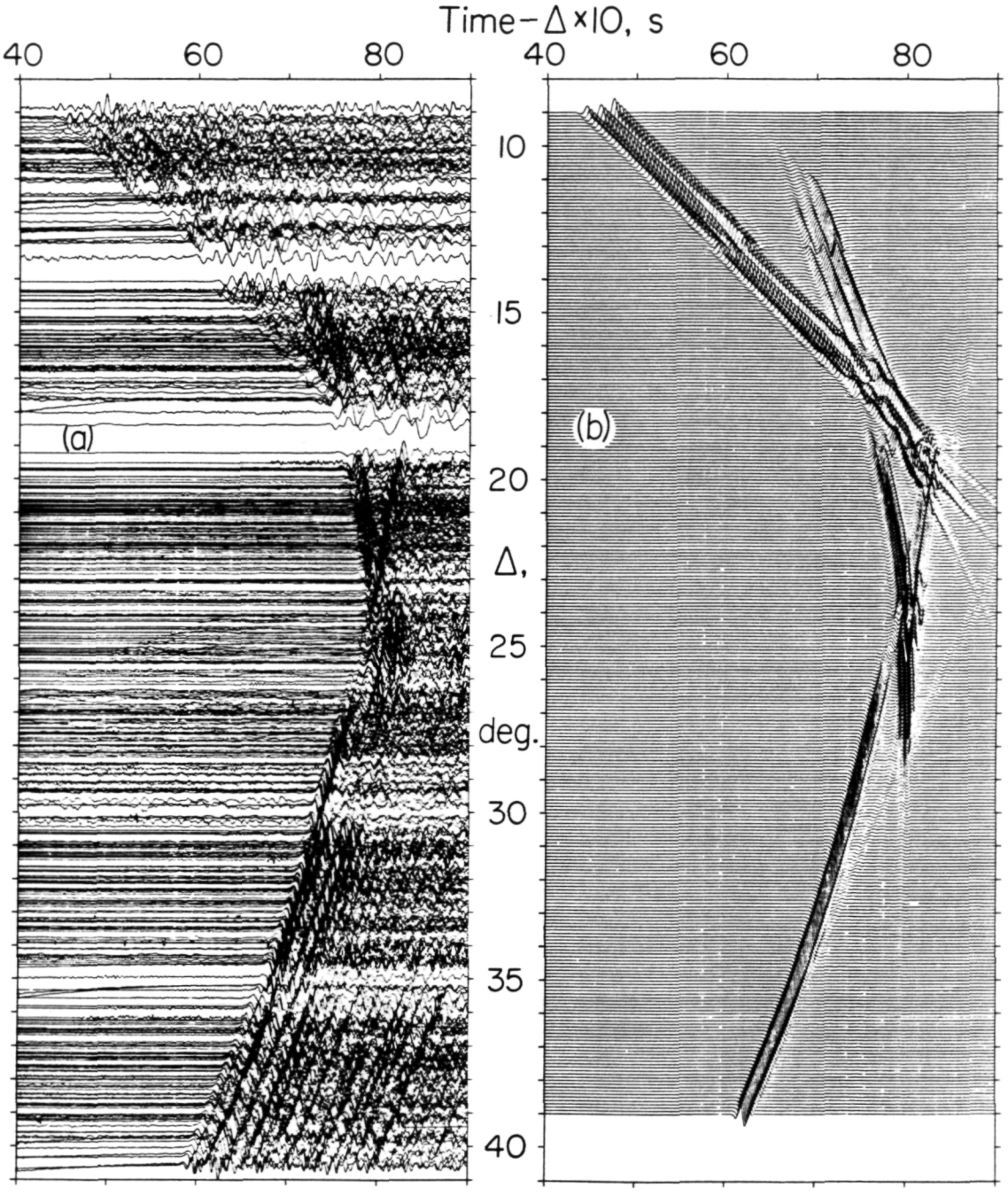

Figure 4

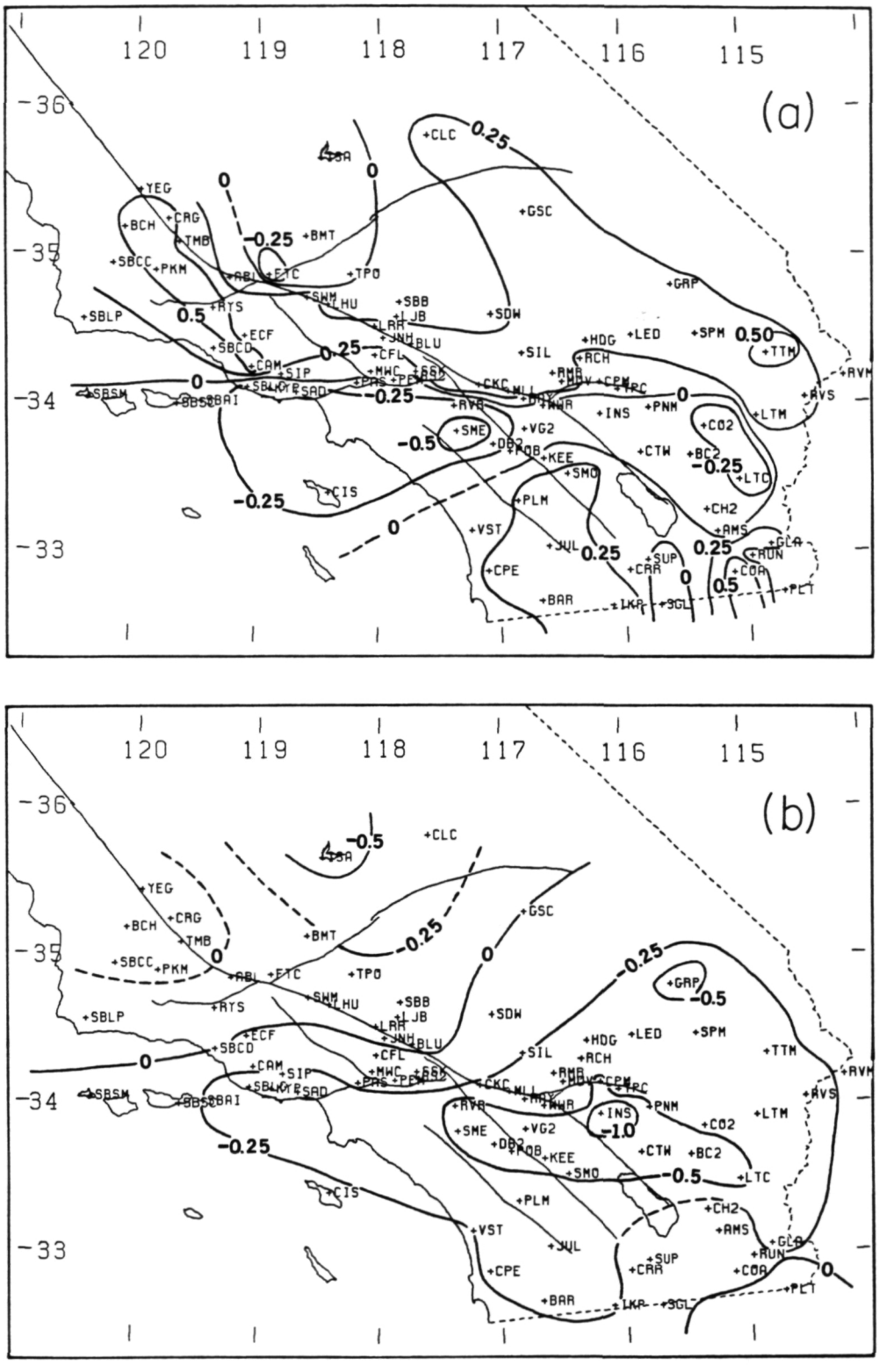
(a)
120
119
118
117
116
115
-36
-35
-34
-33
+CLC
+YEG
+BCH
+CRG
+TMB
+SBCC
+PKM
+BMT
+FTC
+TPO
+GSC
+GRP
+SBLP
+RYS
+ECF
+SBCD
+CAM
+SIP
+SBSM
+SBBR
+SAD
+SBB
+JB
+LAA
+BLU
+CFL
+MWC
+SDW
+SIL
+HDG
+LED
+SPM
+TTM
+RCH
+RMR
+CPM
+IRC
+RVM
+RVS
+INS
+PNM
+LTM
+CO2
+SME
+VG2
+DB2
+TOB
+KEE
+CTW
+BC2
+LTC
+SMO
+CIS
+PLM
+CH2
+AMS
+GLA
+VST
+JUL
+SUP
+CRR
+RUN
+COA
+CPE
+PLT
+BAR
+LKP
+3GL
0.25
0
-0.25
0.5
-0.5
0.50
-1.0

(b)
120
119
118
117
116
115
-36
-35
-34
-33
+CLC
+YEG
+BCH
+CRG
+TMB
+SBCC
+PKM
+BMT
+FTC
+TPO
+GSC
+GRP
+SBLP
+RYS
+ECF
+SBCD
+CAM
+SIP
+SBSM
+SBBR
+SAD
+SBB
+JB
+LAA
+BLU
+CFL
+MWC
+SDW
+SIL
+HDG
+LED
+SPM
+TTM
+RCH
+RMR
+CPM
+IRC
+RVM
+RVS
+INS
+PNM
+LTM
+CO2
+SME
+VG2
+DB2
+TOB
+KEE
+CTW
+BC2
+LTC
+SMO
+CIS
+PLM
+CH2
+AMS
+GLA
+VST
+JUL
+SUP
+CRR
+RUN
+COA
+CPE
+PLT
+BAR
+LKP
+3GL
-0.5
0
0.25
-0.25
-0.5
-1.0

Figure 5

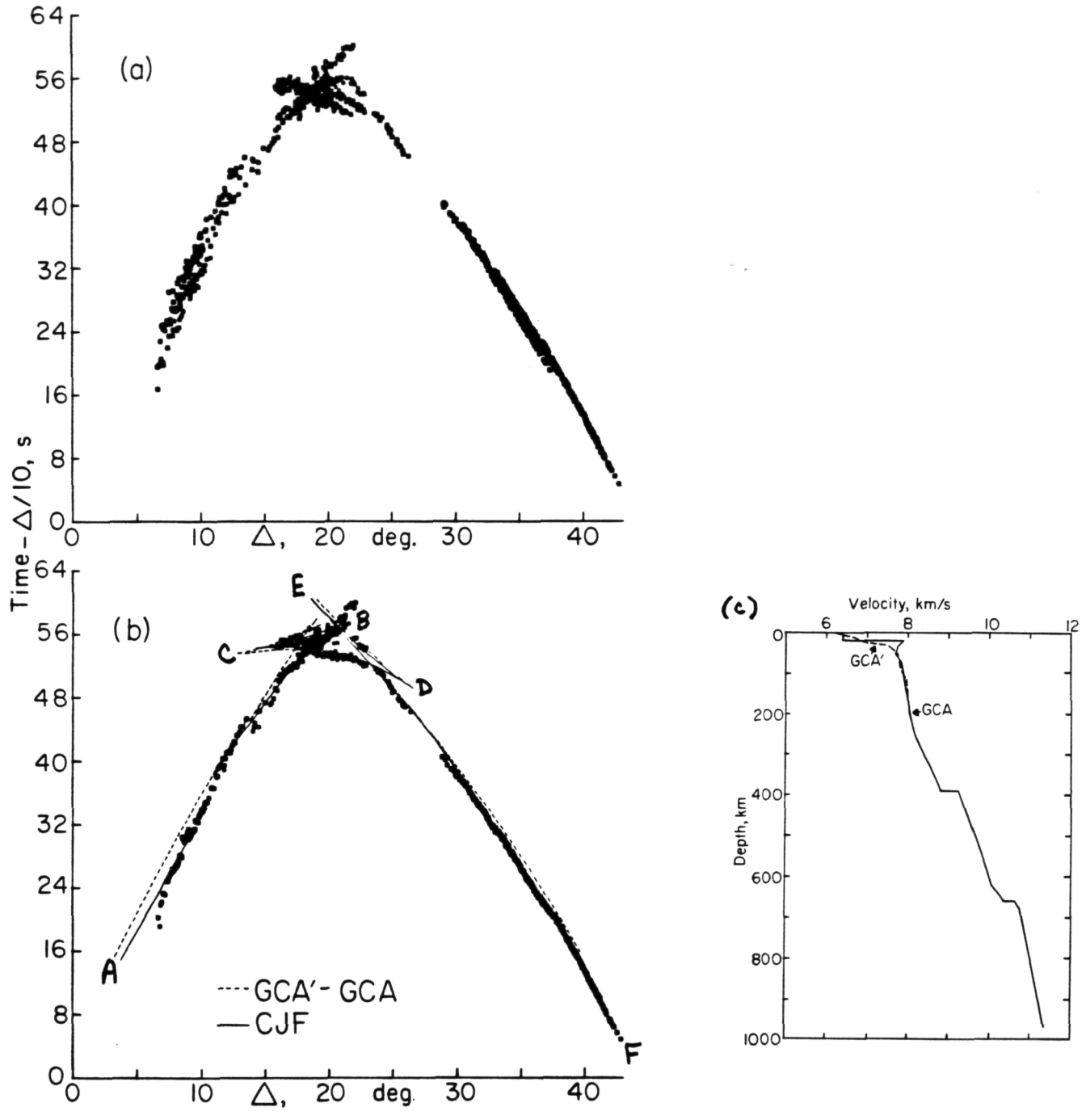
(a)
(b)
(c)
Time-Δ/10, s
Δ, deg.
A
B
C
D
E
F
----GCA'- GCA
—CJF
Velocity, km/s
Depth, km
GCA'
GCA

Figure 6

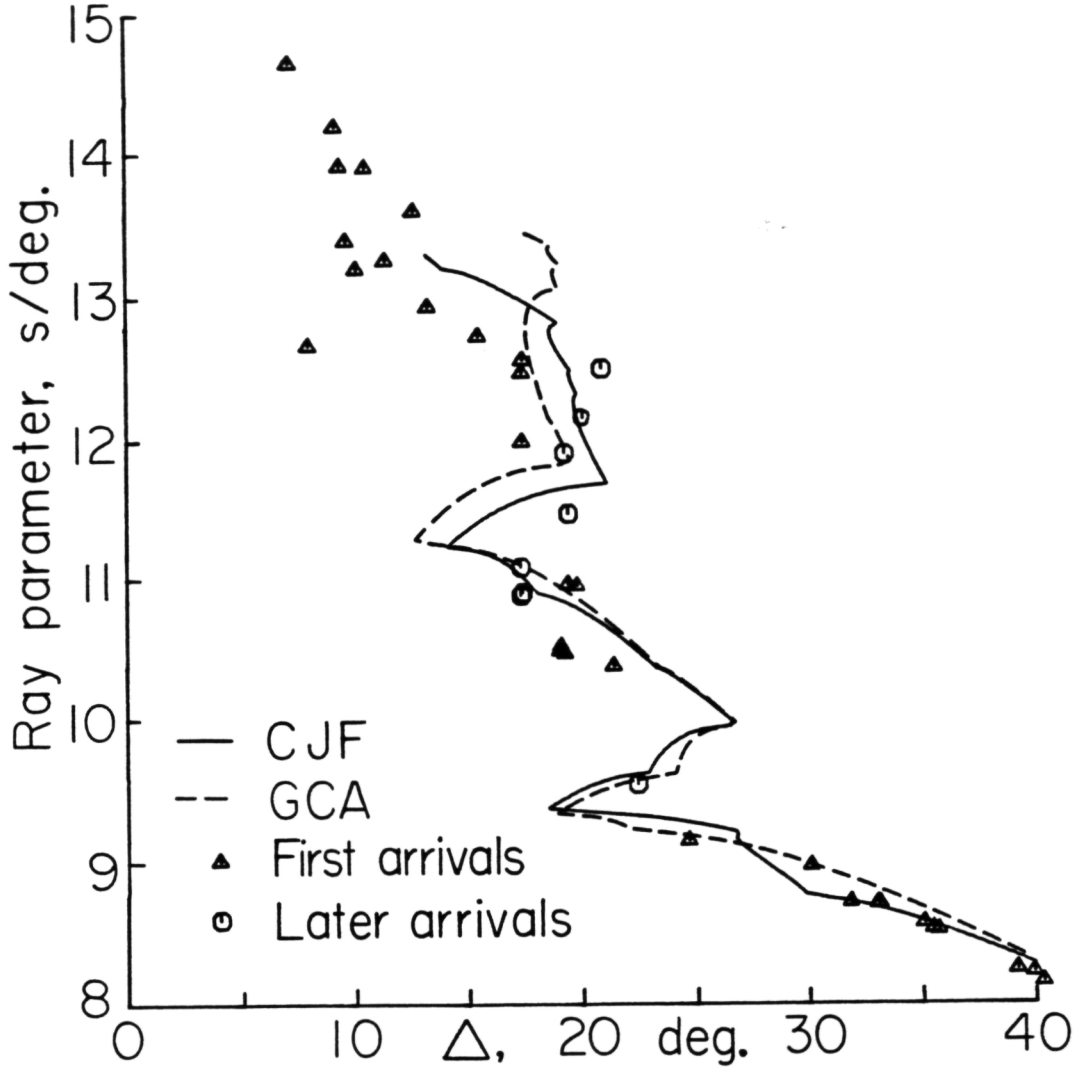
Ray parameter, s/deg.
15
14
13
12
11
10
9
8
0
10
Δ,
20
deg.
30
40
CJF
GCA
First arrivals
Later arrivals

Figure 7

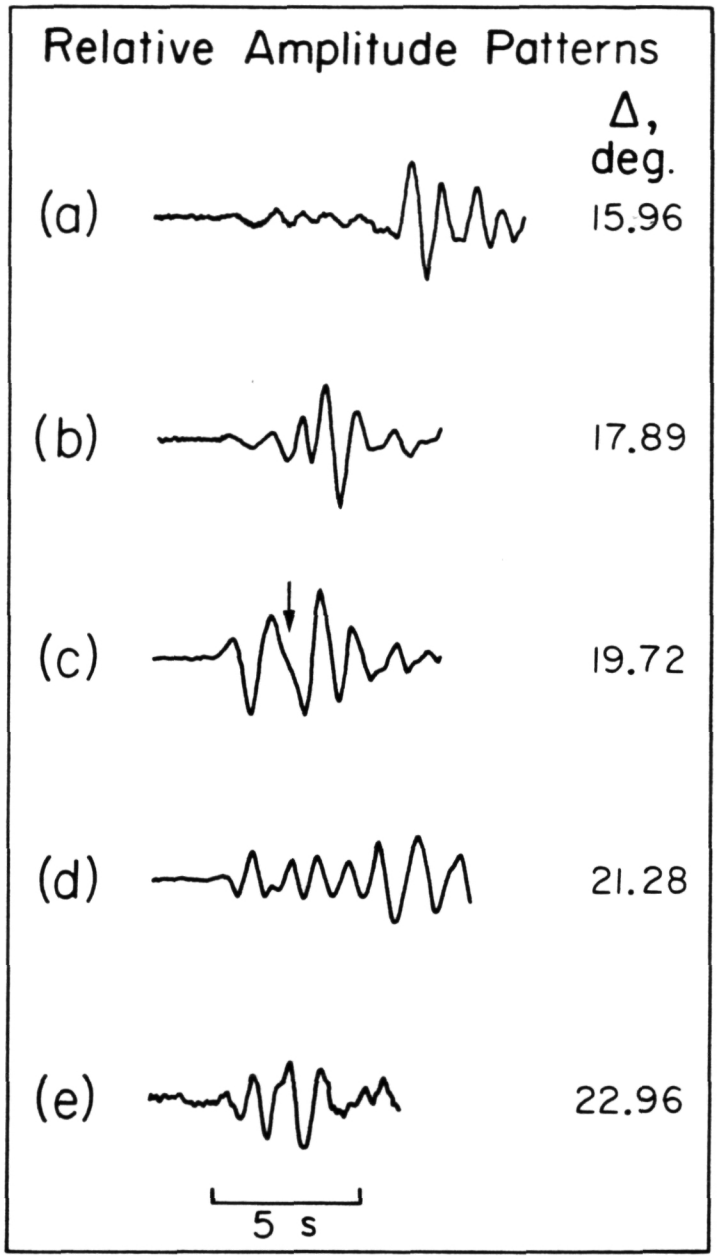
Relative Amplitude Patterns
Δ, deg.
(a)
15.96
(b)
17.89
(c)
19.72
(d)
21.28
(e)
22.96
5 s

Figure 8

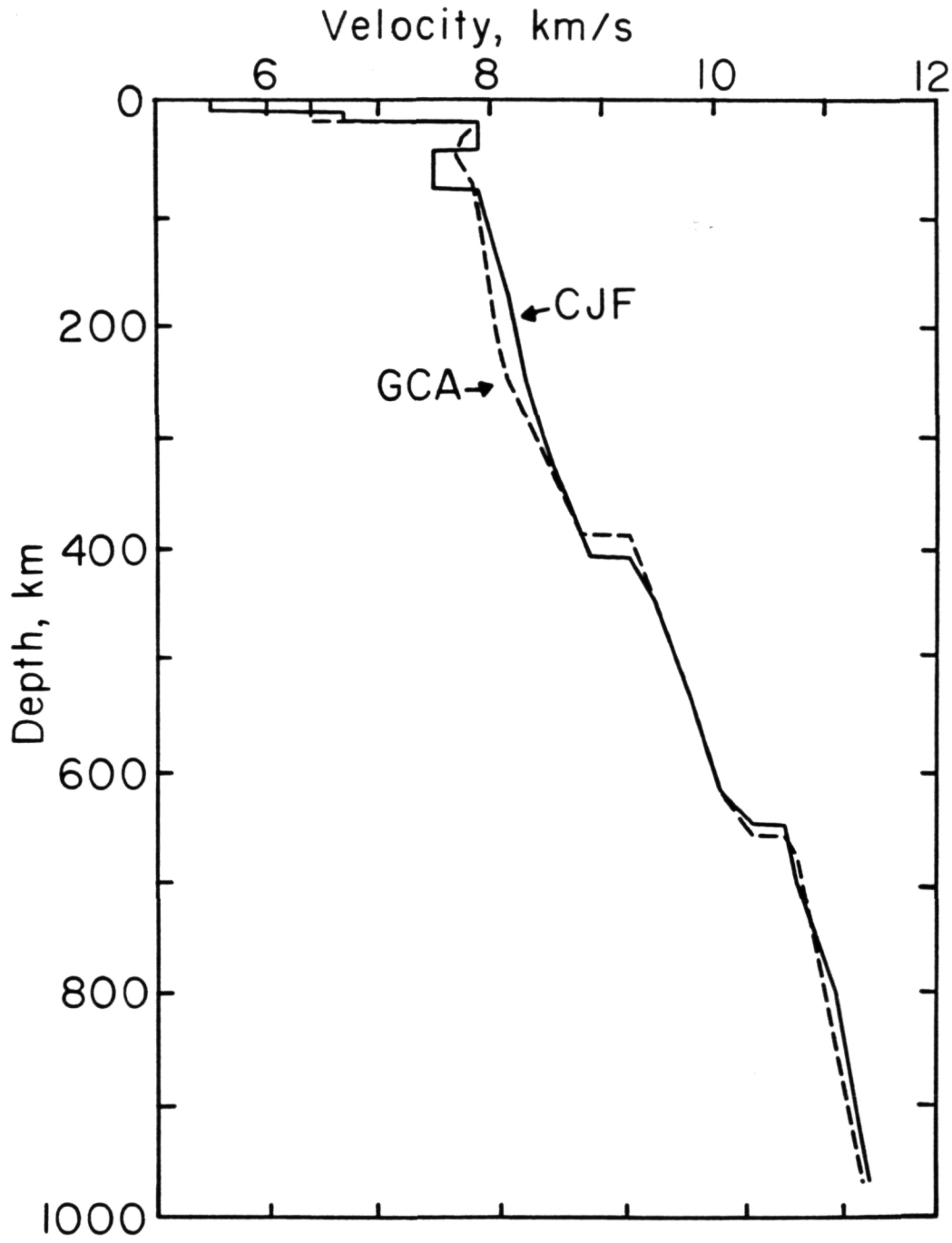

Figure 9

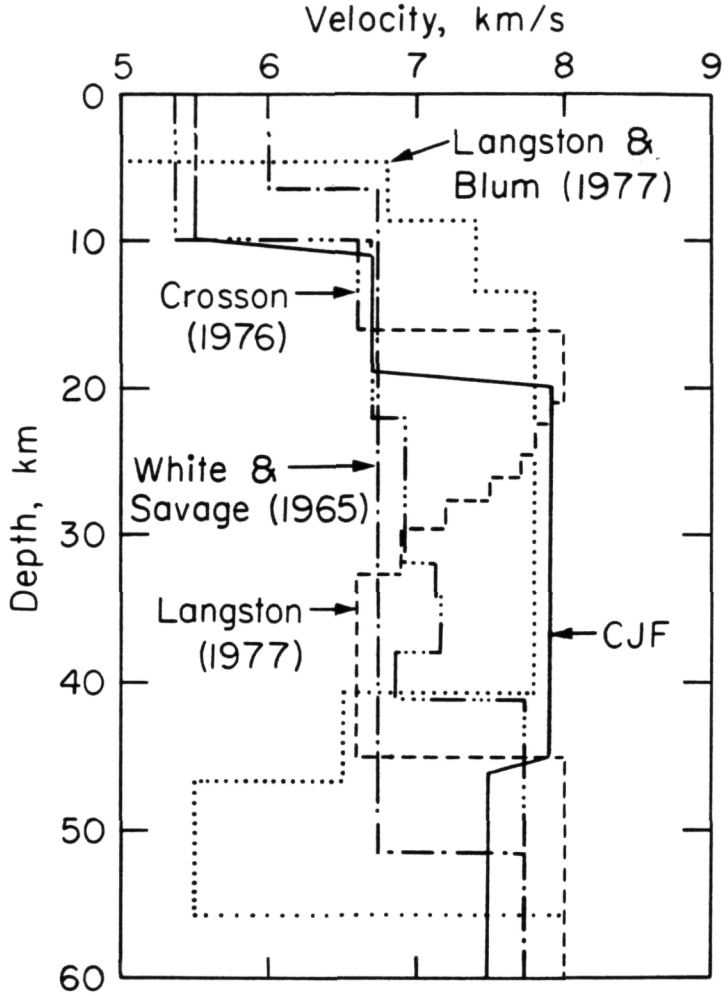
Velocity, km/s
5
6
7
8
9
0
10
20
30
40
50
60
Depth, km
Langston &
Blum (1977)
Crosson
(1976)
White &
Savage (1965)
Langston
(1977)
CJF

Figure 10

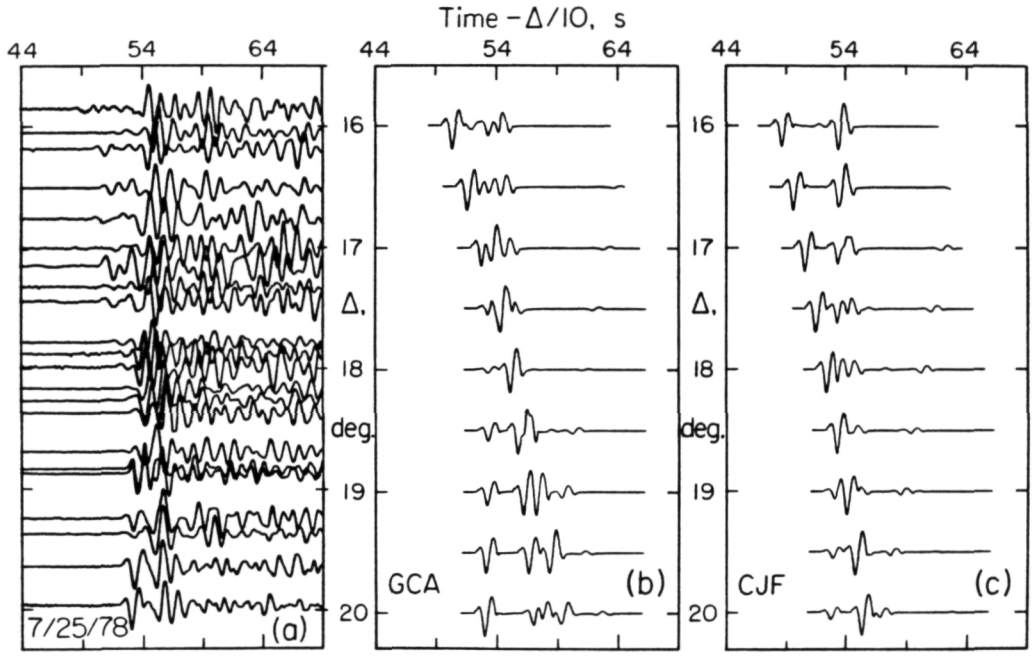

Figure 11

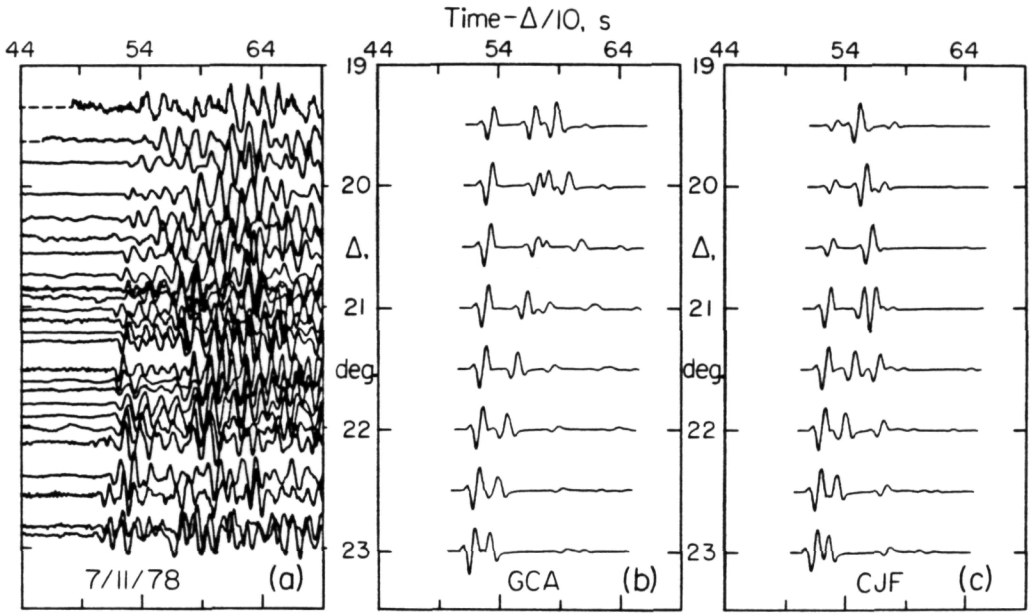

Figure 12

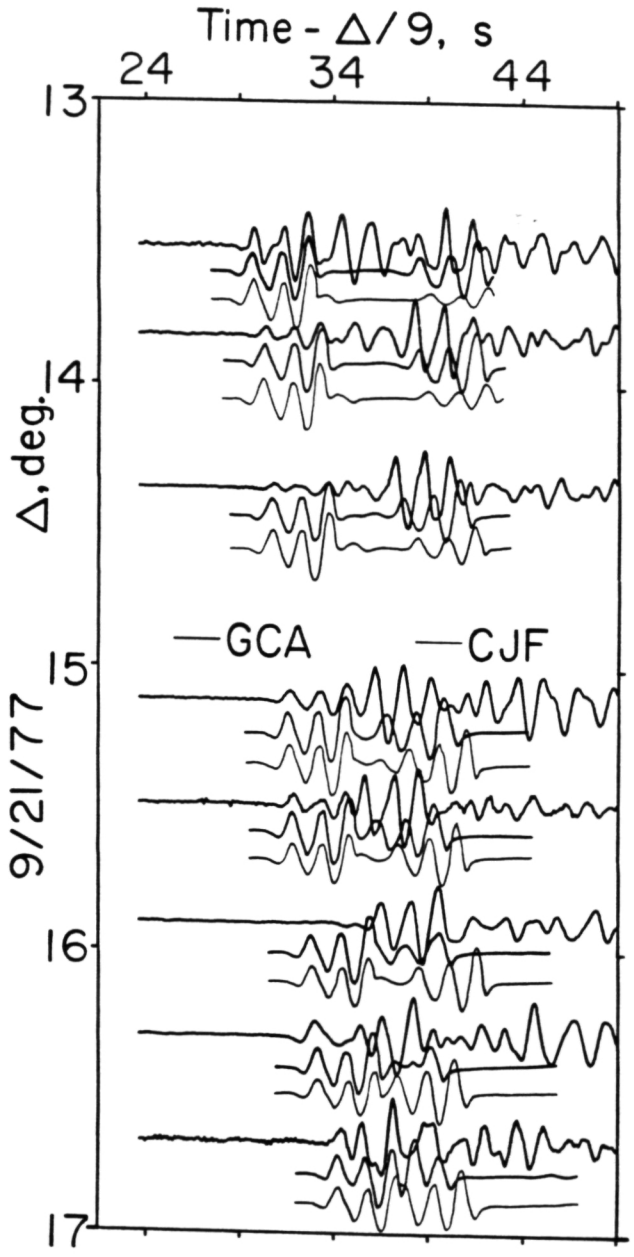

Figure 13

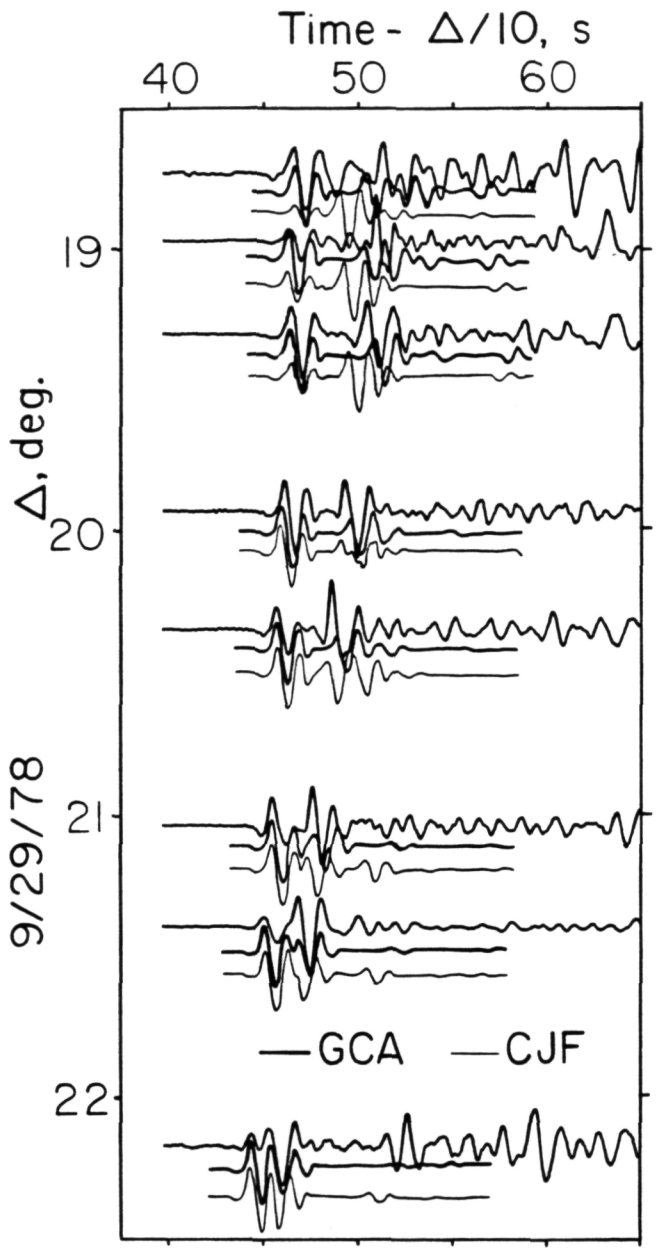

Figure 14

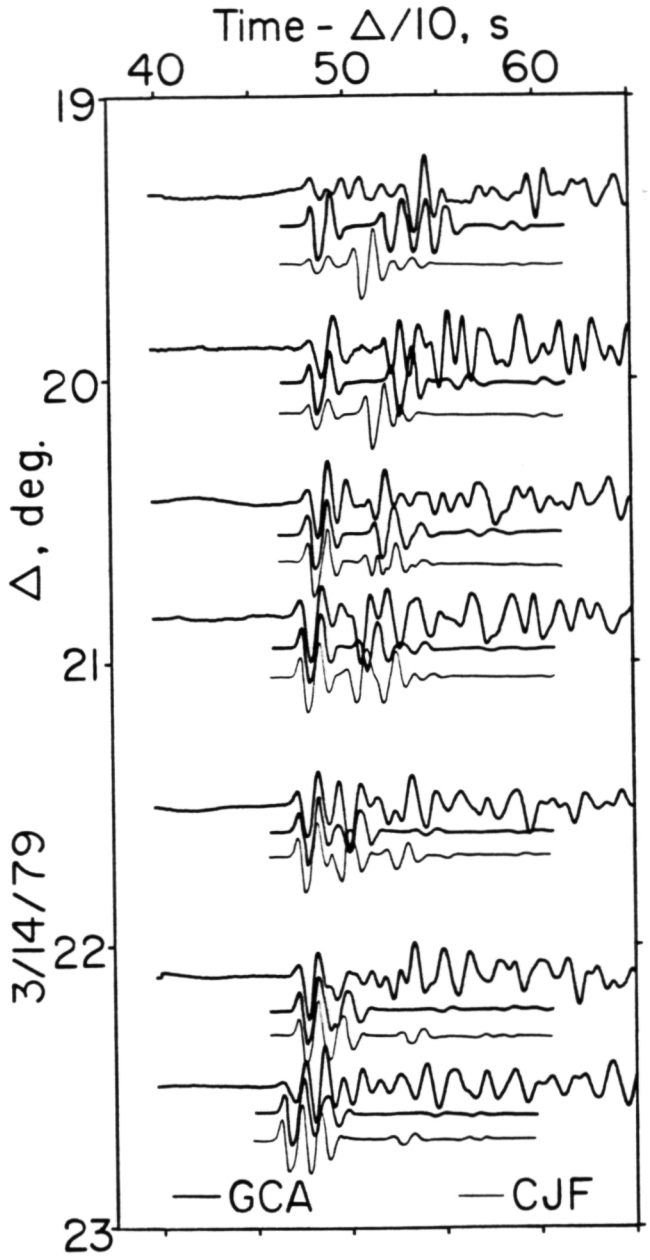

Figure 15

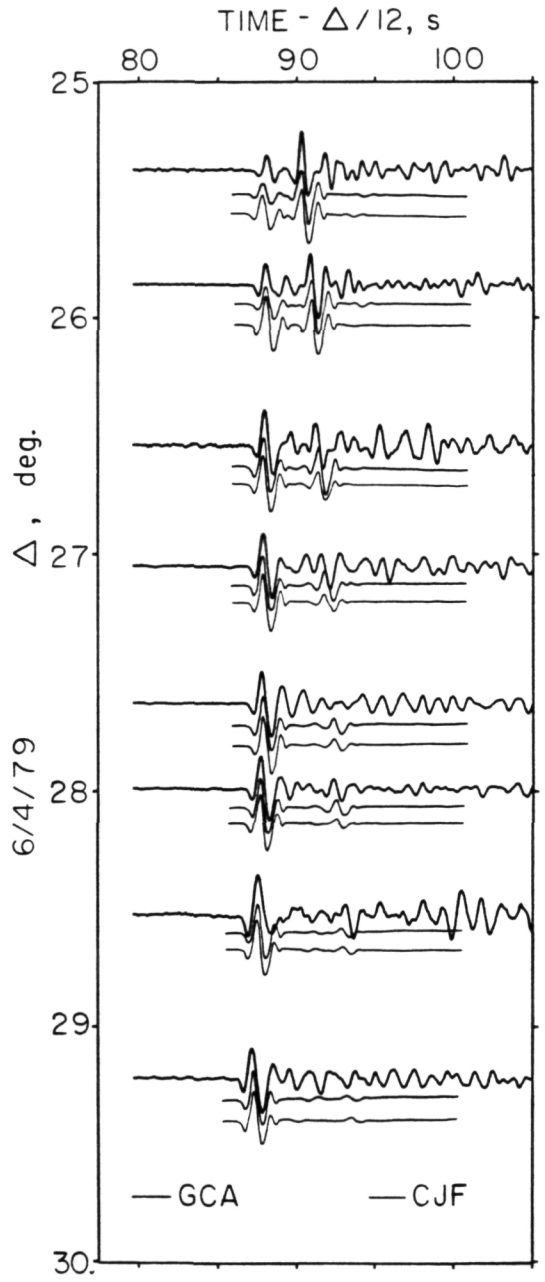

Figure 16

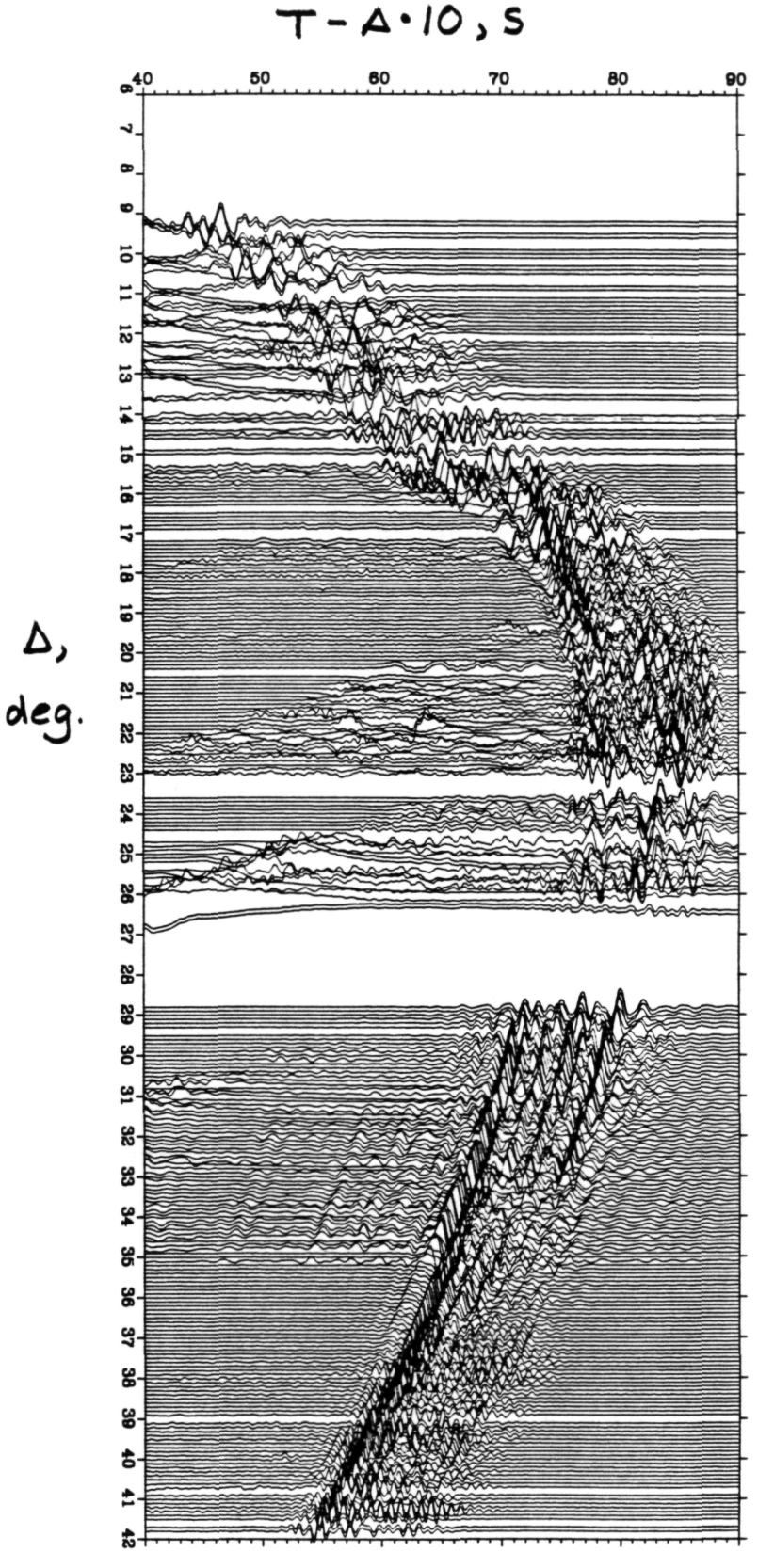
T - Δ·10, S
40
50
60
70
80
90
6
7
8
9
10
11
12
13
14
15
16
17
18
19
20
21
22
23
24
25
26
27
28
29
30
31
32
33
34
35
36
37
38
39
40
41
42
Δ, deg.

Figure 17

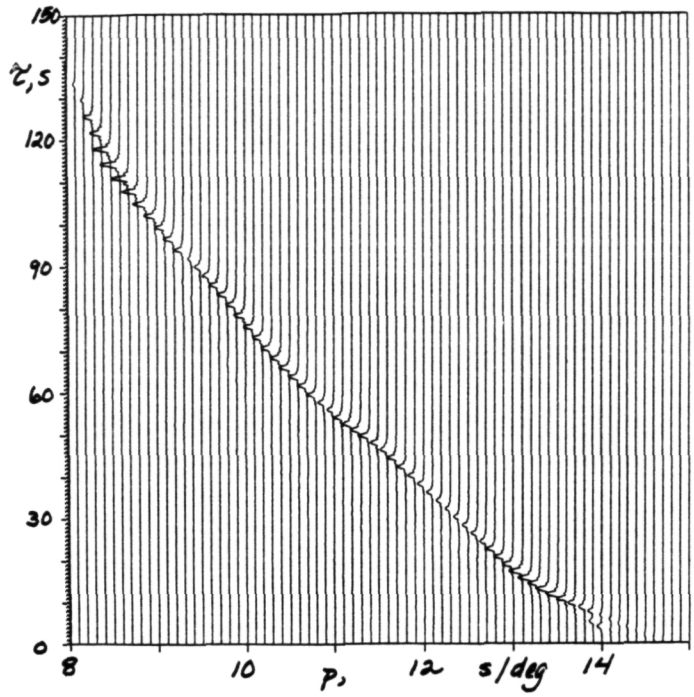

(a)

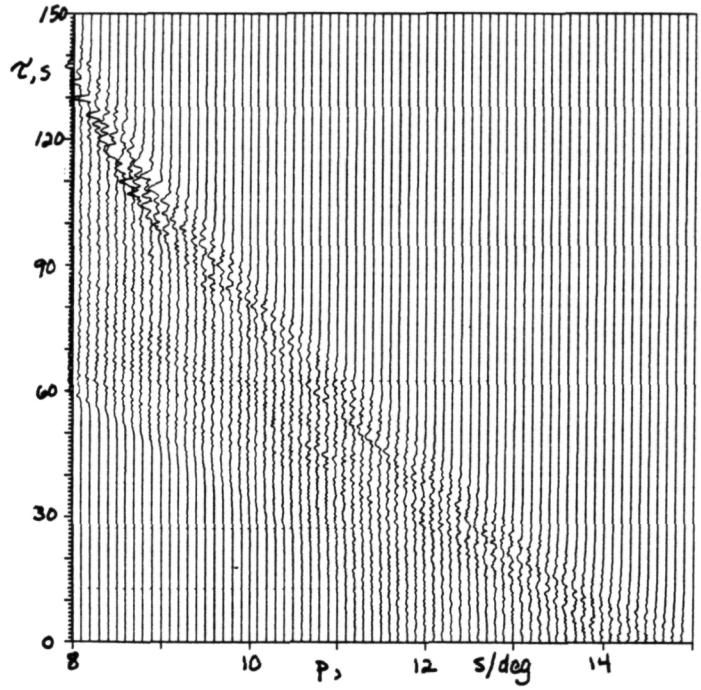

(b)

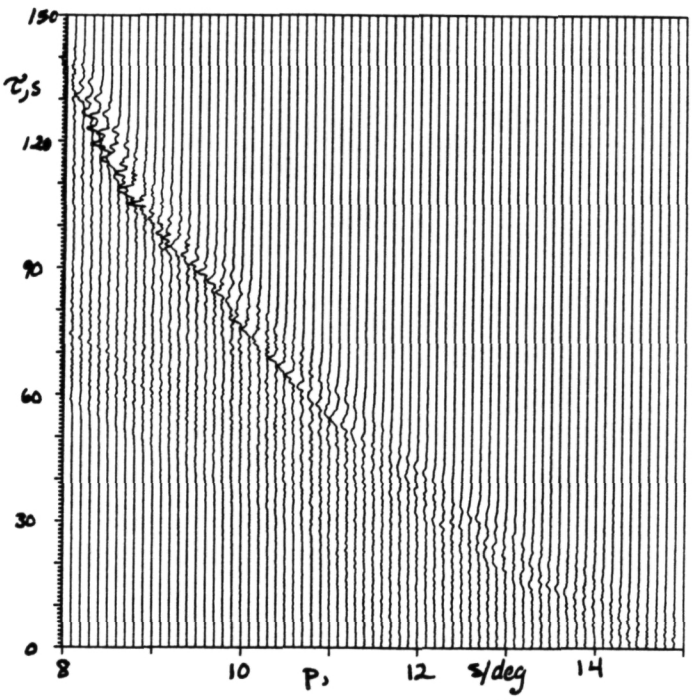

(c)

Figure 18

Radius, km
Depth, km
p, s/deg
(a)

Radius, km
Depth, km
p, s/deg.
(b)

Radius, km
Depth, km
p, s/deg.
(c)

Figure 19

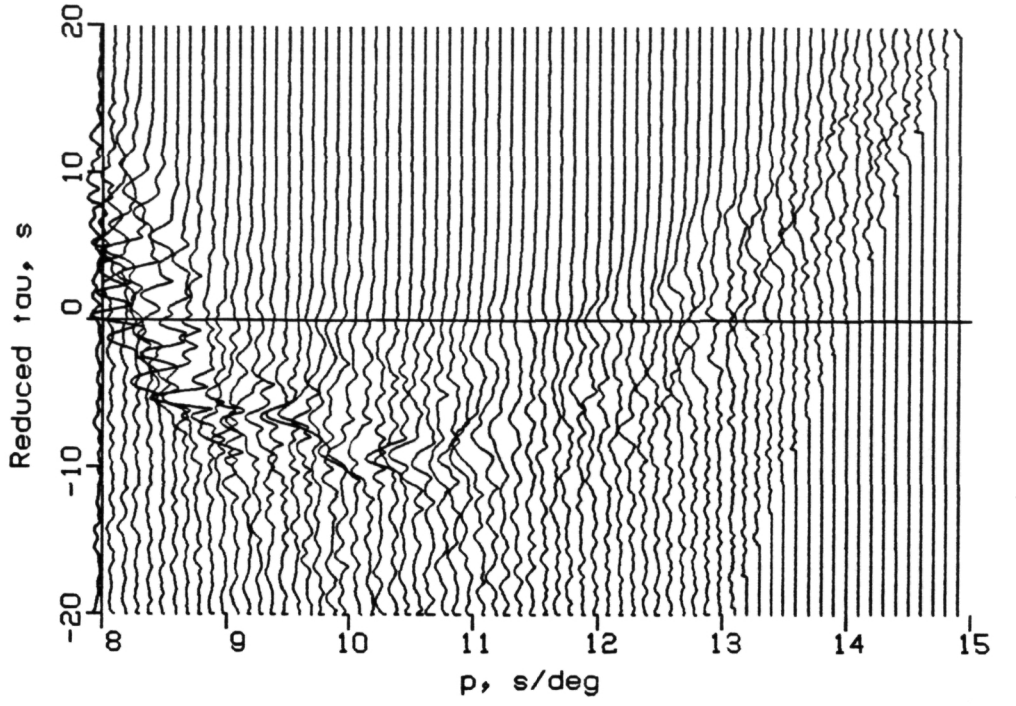

(a)

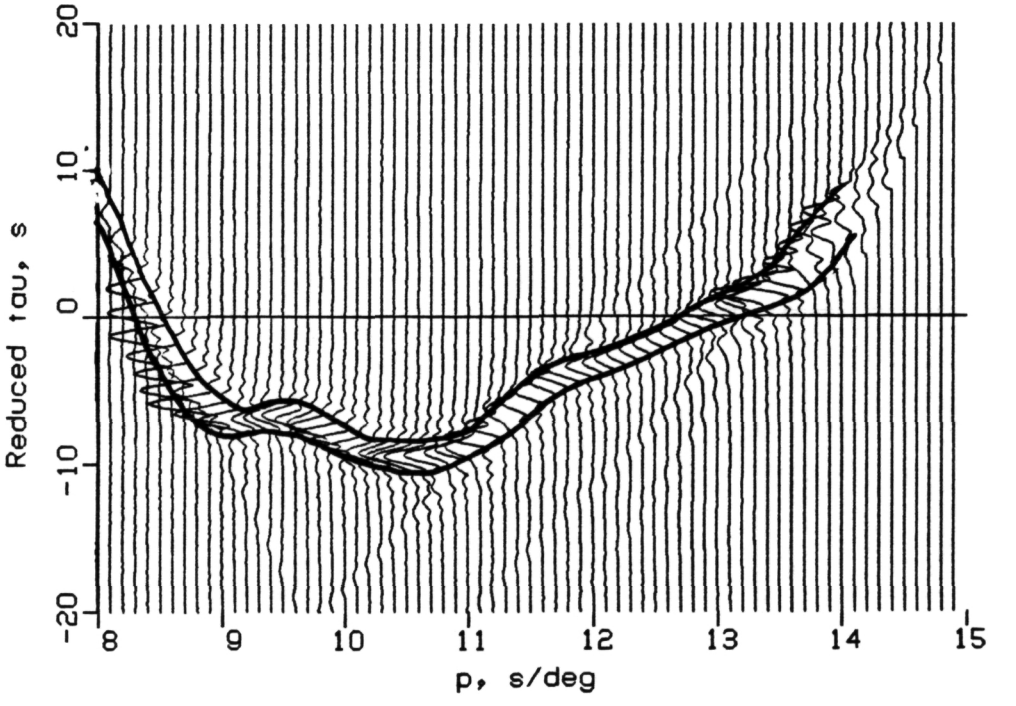

(b)

Figure 20ab

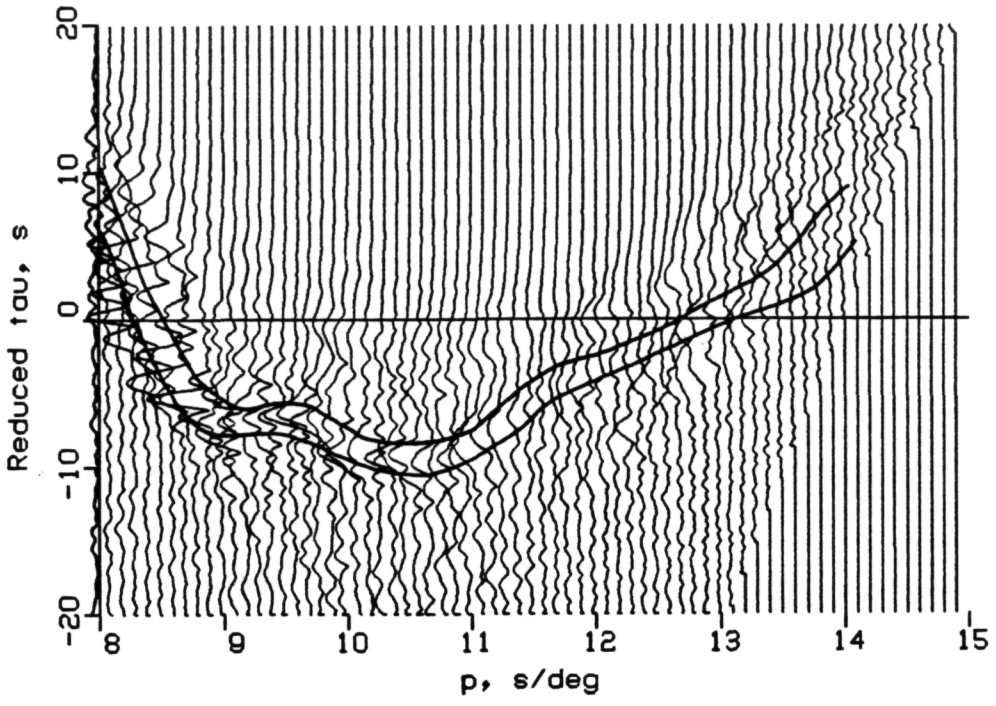

(c)

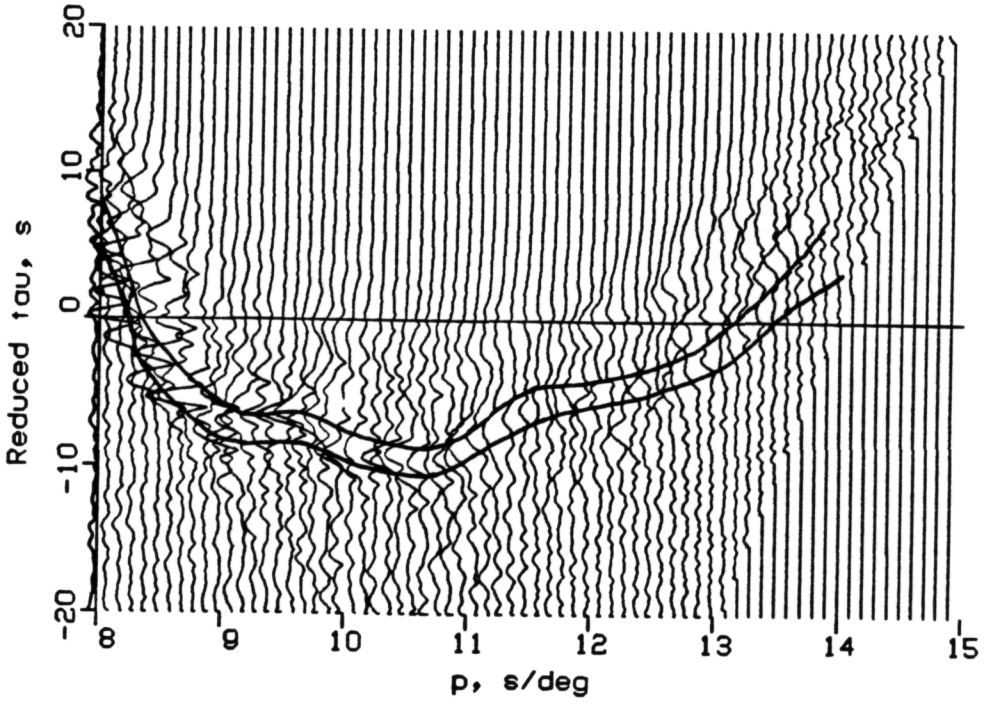

(d)

Figure 20cd

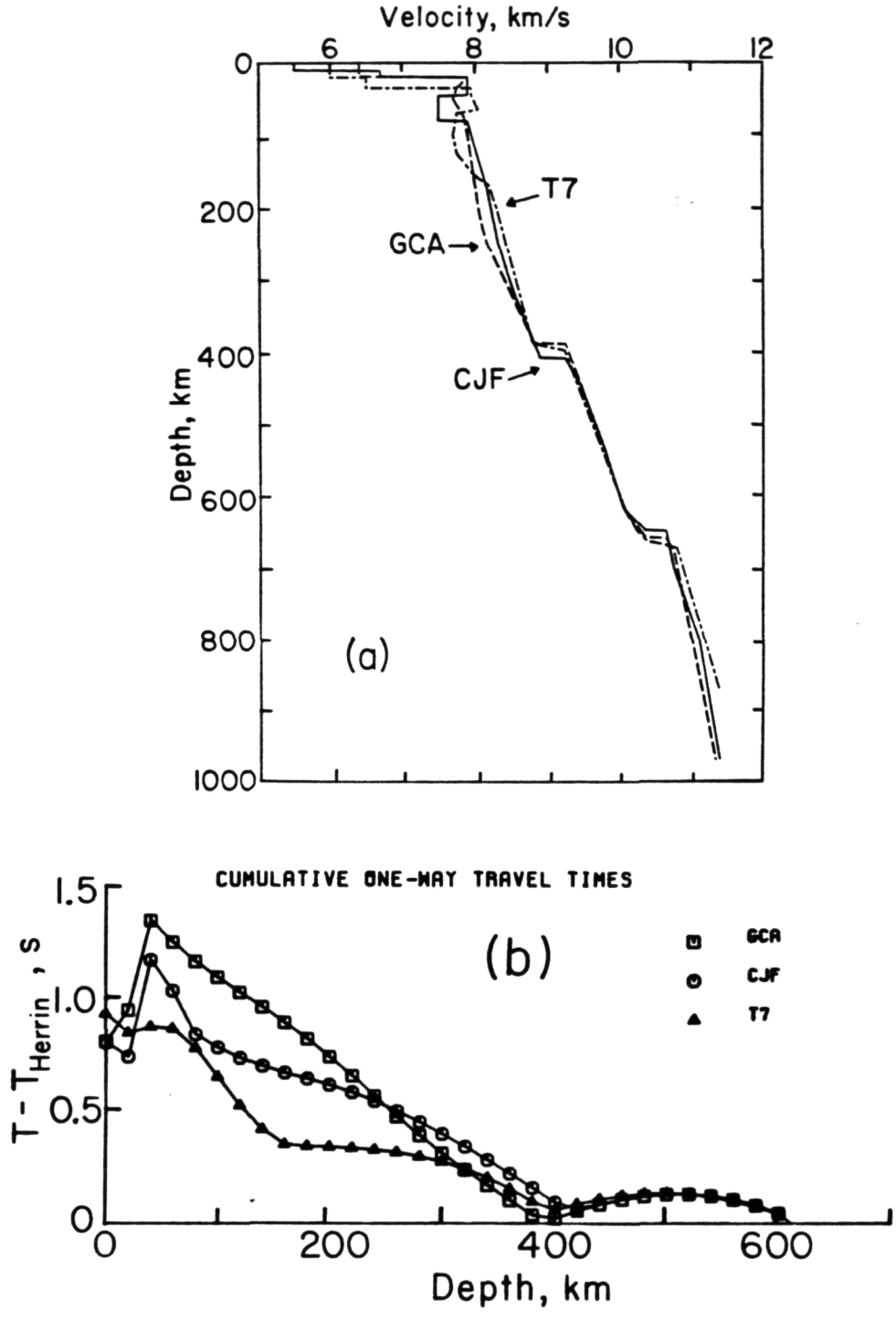
Velocity, km/s
6
8
10
12
0
200
400
600
800
1000
Depth, km
T7
GCA
CJF
(a)
CUMULATIVE ONE-WAY TRAVEL TIMES
(b)
GCA
CJF
T7
1.5
1.0
0.5
0
T - T Herrin , s
0
200
400
600
Depth, km

Figure 21